

## Field Measurements of Surface and Near-Surface Turbulence in the Presence of Breaking Waves

PETER SUTHERLAND\* AND W. KENDALL MELVILLE

*Scripps Institution of Oceanography, La Jolla, California*

(Manuscript received 13 July 2014, in final form 15 December 2014)

### ABSTRACT

Wave breaking removes energy from the surface wave field and injects it into the upper ocean, where it is dissipated by viscosity. This paper presents an investigation of turbulent kinetic energy (TKE) dissipation beneath breaking waves. Wind, wave, and turbulence data were collected in the North Pacific Ocean aboard R/P *FLIP*, during the ONR-sponsored High Resolution Air-Sea Interaction (HiRes) and Radiance in a Dynamic Ocean (RaDyO) experiments. A new method for measuring TKE dissipation at the sea surface was combined with subsurface measurements to allow estimation of TKE dissipation over the entire wave-affected surface layer. Near the surface, dissipation decayed with depth as  $z^{-1}$ , and below approximately one significant wave height, it decayed more quickly, approaching  $z^{-2}$ . High levels of TKE dissipation very near the sea surface were consistent with the large fraction of wave energy dissipation attributed to non-air-entraining microbreakers. Comparison of measured profiles with large-eddy simulation results in the literature suggests that dissipation is concentrated closer to the surface than previously expected, largely because the simulations did not resolve microbreaking. Total integrated dissipation in the water column agreed well with dissipation by breaking for young waves,  $c_m/u_* < 50$  (where  $c_m$  is the mean wave frequency and  $u_*$  is the atmospheric friction velocity), implying that breaking was the dominant source of turbulence in those conditions. The results of these extensive measurements of near-surface dissipation over three field experiments are discussed in the context of observations and ocean boundary layer modeling efforts by other groups.

### 1. Introduction

When wind flows over the open sea, it creates surface waves. Energy, momentum, and mass flux between the atmosphere and ocean are all modulated by this wave field (Melville 1996). Although some of the energy and momentum flux input by the wind propagates away as swell, the majority is injected into the water column locally. This results in a turbulent marine boundary layer near the ocean surface, where energy is dissipated by turbulence. This work uses a combination of subsurface measurements and a newly developed technique for measuring turbulence at the surface (Sutherland and Melville 2015, manuscript submitted to *J. Atmos. Oceanic Technol.*,

hereinafter SM15) to investigate dissipation in this boundary layer.

The simplest description of the upper-ocean boundary layer is that of a wall layer, where shear production of turbulence is balanced by dissipation, and the only relevant length and velocity scales are depth  $z$  and friction velocity (in the water)  $u_{*w}$ . This results in a layer of near-surface turbulent kinetic energy (TKE) dissipation with a depth dependence proportional to  $z^{-1}$ . However, since the 1980s, there has been considerable evidence in the literature that TKE dissipation near the surface is greater than that predicted by a wall layer (Kitaigorodskii et al. 1983; Gargett 1989; Agrawal et al. 1992; Anis and Moum 1992; Drennan et al. (1996); Terray et al. (1996); Soloviev and Lukas 2003; Gemmrich 2010). That increased dissipation is thought to be the result of wave breaking (e.g., Melville 1994).

Craig and Banner (1994) addressed this elevated dissipation by theorizing that near-surface turbulence should be the result of a balance between downward diffusion, shear production, and dissipation. They described a two-layer solution where, near the surface, downward diffusion of

\* Current affiliation: Laboratoire d'Océanographie et du Climat, Université Pierre et Marie Curie, Paris, France.

Corresponding author address: Peter Sutherland, Laboratoire d'Océanographie et du Climat, Université Pierre et Marie Curie, 4 Place Jussieu, Paris 75005, France.  
E-mail: peter.sutherland@locean-ipsl.upmc.fr

TKE balances dissipation and dissipation  $\varepsilon$  depends on depth as  $\varepsilon \propto z^{-3.4}$ . Below that layer, shear production balances dissipation resulting in a classical log layer. The crossover depth between these two layers depends on a surface roughness length  $z_0$ , which is still not well understood.

More recent large-eddy simulations (LES) have sought to better capture the effects of wave breaking on the upper ocean. Sullivan et al. (2004, 2007) modeled individual breaking waves as body forces, based on the laboratory measurements of Rapp and Melville (1990) and Melville et al. (2002). They then used an ensemble of breakers, with probability distributions based on the field measurements of Melville and Matusov (2002), to investigate their impact on the dynamics of the upper ocean. They found that the magnitude and vertical distribution of dissipation depend on breaking, that enhanced near-surface dissipation was primarily the result of wave breaking, and that in strong forcing conditions, Langmuir turbulence could transport breaking-generated turbulence to the bottom of an entraining mixed layer.

One region where considerable uncertainty remains is the very near-surface region. Recent work (Sutherland and Melville 2013) has highlighted the importance of microbreaking for energy dissipation. Using their results, section 3 of this paper shows that between 20% and 90% of dissipation by breaking can be attributed to microbreakers. Unless it is advected downward by other processes, like Langmuir turbulence as described above, the turbulence associated with those waves would be constrained to the top  $O(10)$  cm of the water column.

Field measurements of dissipation profiles near the surface have found a wide variety of amplitudes and depth dependencies. For example, Gargett (1989) found  $\varepsilon \propto z^{-4}$  in stormy weather and  $\varepsilon \propto z^{-1}$  in decreasing winds; Terray et al. (1996, hereinafter T96) and Drennan et al. (1996, hereinafter D96) found  $\varepsilon \propto z^{-2}$ ; Soloviev and Lukas (2003) observed profiles that varied from  $\varepsilon \propto z^{-1}$  at depths  $O(H_s)$  to  $\varepsilon \propto z^{-2}$  nearer to the surface (where  $H_s$  is the significant wave height); Gemmrich (2010) observed  $\varepsilon \propto z^{-1}$  with a rapid increase above that in the top few centimeters; and Sutherland et al. (2013), using profiling instruments, generally found dissipation profiles consistent with a  $z^{-1}$  wall layer but also observed exponential dissipation profiles under some wind conditions.

Environmental conditions varied widely over the datasets used by different authors in the literature. Experiments range from offshore measurements in North Pacific storms (Gargett 1989) to highly controlled measurements taken on sheltered lakes (Gemmrich 2010). A nondimensional scaling of these data that collapses all dissipation profiles to a single curve has not yet been found.

Measurements very near the sea surface, within  $O(10)$  cm, were not possible with the instrumentation

used by most authors in the literature. Recent work by Gemmrich (2010) and Thomson (2012) attempted to access this region using upward-pointing pulse-coherent acoustic Doppler profilers (PCADPs), but accurate estimates of dissipation using their processing techniques required averaging over a larger depth range.

The broad scatter of results in the literature is likely, at least in part, because of the great difficulty in making measurements of turbulence near a wavy surface. The primary problem is that velocity fields of waves and turbulence near the sea surface inhabit the same range of scales and must be separated. Instruments measuring turbulence in a wavy environment are also susceptible to measuring their own turbulent wake as it is advected past them by successive waves.

Reconciling dissipation by breaking with measured water column dissipation remains a significant problem in the literature (Rascle et al. 2013). The intention of our work is to use a combination of new measurements and techniques to address that problem, particularly in the top  $O(10)$  cm of the water column.

To better resolve TKE dissipation very near the surface, and to address the instrumentation issues described above, SM15 presented a new nonintrusive technique, using stereo infrared imagery, for the separation of waves and turbulence at the sea surface. They were then able to measure TKE dissipation directly at the surface. Since the instrumentation was remote, it did not produce a turbulent wake in the water.

In this paper, the surface measurements of SM15 have been combined with an array of subsurface PCADP devices to measure TKE dissipation from depths of several significant wave heights up to the sea surface. This allows us to measure the depth dependence of dissipation and to constrain depth-integrated TKE dissipation over the upper wave-affected surface layer.

The paper is organized as follows: Section 2 describes field measurements, including the platform, instrumentation, field sites, conditions, and the computation of wave field statistics. Statistics of breaking waves are discussed in section 3. Surface TKE dissipation measurements are described in section 4. Subsurface measurements of TKE dissipation and the technique used to calculate them are described in 5. Section 6 is a discussion of the results. This includes a comparison of measured dissipation profiles with those found in the literature and a comparison of vertically integrated dissipation with dissipation by wave breaking. The discussion section also covers the wave coherence of dissipation and the results of sampling an intermittent process. Conclusions of the paper are presented in section 7. Three appendixes are

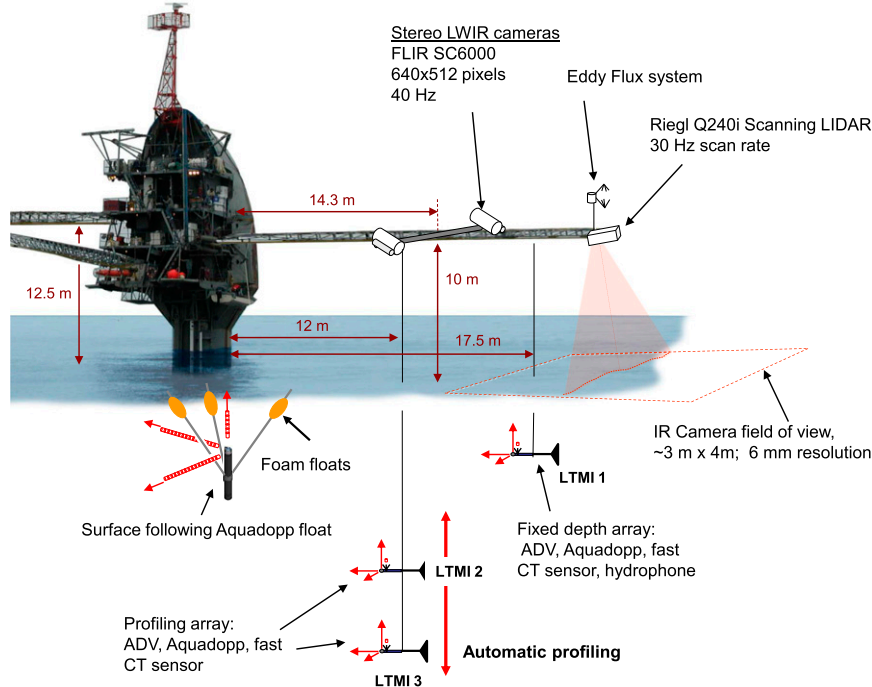


FIG. 1. Schematic of the instrument configuration aboard R/P *FLIP* during the SoCal 2010 experiment. The configuration during the RaDyO 2009 experiment was similar, but instruments were mounted on the opposite (port) boom. During HiRes 2010, LTMIs were not deployed.

also included: [Appendix A](#) describes the processing of Aquadopp PCADP data, [appendix B](#) discusses the effects of instrument wakes, and [appendix C](#) provides definitions of energy flux.

## 2. Field measurements

The data described here were collected during three deployments of the Research Platform (R/P) *Floating Instrument Platform (FLIP)* in the Pacific Ocean in 2009 and 2010. *FLIP* was chosen as a platform because of its stability ([Smith and Rieder 1997](#)) and small waterplane, which minimizes reflection and shadowing of the wave field. Further, *FLIP* also has a small superstructure for minimal airflow distortion and long booms to hold instruments well away from the flow-distorted regions ([Mollo-Christensen 1968](#)).

### a. Instrumentation

Each of the three experiments differed slightly in the instruments deployed and their configuration. [Figure 1](#) shows a schematic of the instrument setup during the Southern California (SoCal) 2010 experiment. The Radiance in a Dynamic Ocean (RaDyO) 2009 instrument suite was similar but installed on the port boom (instead of the starboard boom as shown in [Fig. 1](#)).

Measurements of the sea surface morphology and velocity field were taken with a stereo pair of long-wave infrared ( $8\text{--}9.2\ \mu\text{m}$ ) video cameras, mounted 3 m apart on a horizontal spar at the end of one of *FLIP*'s booms and angled slightly toward each other so that they shared the same field of view on the sea surface. The collocated field of view was approximately  $4\ \text{m} \times 3\ \text{m}$ , and the image size of  $640 \times 512$  pixels resulted in a nominal resolution of approximately 6 mm. IR video was captured at 40 Hz and subsampled to 20 Hz for the first 20 min of every hour. This arrangement provided a reconstruction of the sea surface shape at approximately 5-cm resolution at 20 Hz and the 3D velocity of the surface water at approximately 5-cm resolution at a further subsampled 4 Hz.

Subsurface turbulence was measured with an array of lowered turbulence measurement instruments (LTMIs). Up to three LTMIs were deployed, with one at a fixed depth and two profiling. The uppermost LTMI was held at a fixed depth, relative to the mean surface, and located at the end of one of *FLIP*'s booms (approximately 16 m from *FLIP*'s hull), directly beneath the IR cameras' fields of view. The lower two LTMIs were mounted inboard along the same boom at approximately 10.5 m from *FLIP*'s hull, and their depths (relative to the mean surface) were changed every 10 or 20 min.

Each LTMI consisted of a pulse-coherent acoustic Doppler profiler (Nortek 2-MHz Aquadopp HR Profiler),

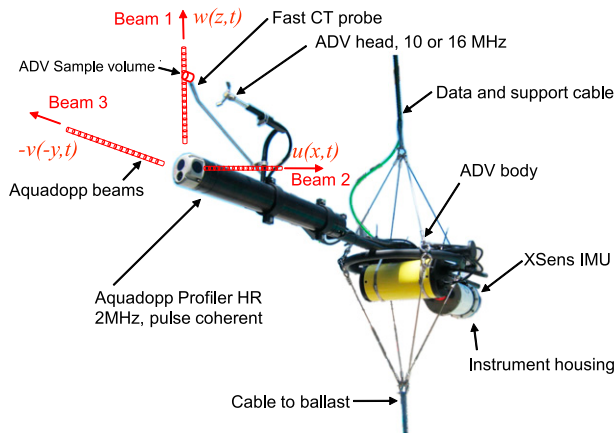


FIG. 2. Subsurface LTM. Not shown is a vane designed to keep the body of the Aquadopp orthogonal to the mean flow, with beam two pointing upstream. Instruments with vane attached are shown in Fig. 3.

an acoustic Doppler velocimeter (ADV; Nortek Vectrino, Sontek MicroADV, or Nortek Vector), a fast conductivity–temperature probe (PME 9028), and inertial motion unit (XSens MTi). Figure 2 shows one of the profilers, demonstrating the relative configuration of the instrumentation. The apparatus was designed to keep the sampling volume of the Aquadopp as far as possible from the wake of the instrument body and supporting cables. The LTMs were vanned (Fig. 3) so that each Aquadopp was on the upstream side, with one beam pointing directly into the mean current and two beams orthogonal to the current direction, with one pointing directly upward. The behavior of the LTMs in a variety of sea states and current conditions was observed, both visually and by observing the IMU record, and the instruments were found to be directionally stable. To assist with resolving velocity ambiguities in the Aquadopp records, each ADV was mounted such that its sampling volume (but not the instrument itself) was collocated with beam one of the Aquadopp profilers. This allowed the use of the ADV for the elimination of velocity ambiguities due to phase wrapping in the Aquadopp data.

An additional Aquadopp was mounted pointing upward on a surface-following float (shown in Fig. 1). This float was loosely tethered to one of *FLIP*'s booms, allowing the instrument to move in approximately the reference frame of the orbital motions of larger waves. This reduced the instrument wake generated by wave orbital motions and allowed the Aquadopp to keep the water surface continuously within its vertical beam. Although not directly collocated with the field of view of the stereo IR cameras (it typically drifted approximately 10-m downwind), by assuming statistical homogeneity over the separation scale, meaningful comparisons can be made.

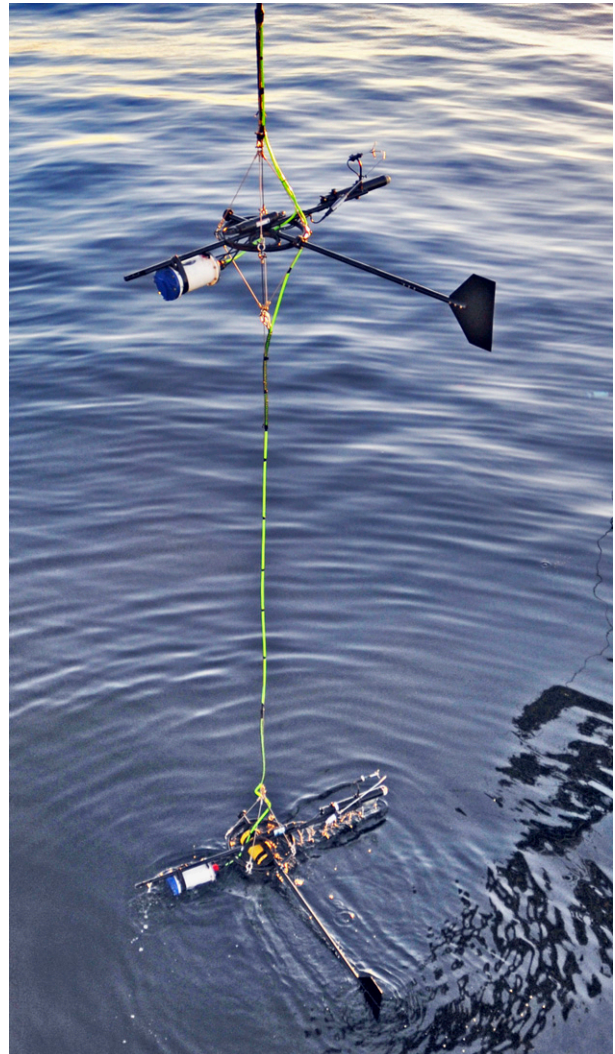


FIG. 3. Profiling LTMs numbers two and three suspended below the starboard boom of *FLIP* just prior to deployment in the SoCal 2010 experiment. Both instruments pivot independently about the data and support cable (green) and are directed into the mean current by the black vanes. The natural orientation in a current is to have the crossbar holding the instrumentation orthogonal to the direction of flow and the vane pointing downstream. It is worth noting the reflection of the boom that can be seen on the sea surface at the lower right of the figure. The stereo IR cameras were mounted at the end of the boom, angled outwards in order to avoid contaminating the imagery with this reflection.

In all three experiments, a Campbell Scientific eddy flux system (CSAT3 3D sonic anemometer) was mounted directly over the IR cameras' common field of view. These data were processed to retrieve Reynolds stresses, wind speed, and wind direction (Grare et al. 2013).

#### b. Field sites

Three experimental locations were chosen to provide a wide range of experimental conditions; the trade

wind-dominated region south of Hawaii, the strong alongshore winds off Northern California, and the relatively mild conditions in the Southern California Bight.

The first experiment, RaDyO 2009 (Dickey et al. 2012), was a 12-day deployment that started 120 km south of the island of Hawai'i with *FLIP* drifting west at approximately  $35 \text{ cm s}^{-1}$  for approximately 330 km. Conditions were typical trade winds (Figs. 4a–c) with 10-m winds  $U_{10}$  ranging between 4 and  $12 \text{ m s}^{-1}$  from the east and significant wave heights  $H_s$  between 1.5 and 2.5 m.

The ONR-sponsored High Resolution Air-Sea Interaction (HiRes) Departmental Research Initiative (DRI) consisted of two experiments: HiRes 2010 was a 14-day deployment with *FLIP* moored approximately 25 km off the coast of northern California ( $38^{\circ}20'N$ ,  $123^{\circ}26'W$ ) in generally strong northwesterly winds. Wind speeds  $U_{10}$  were from 1 to  $17 \text{ m s}^{-1}$ , and significant wave heights ranged from 1 to 5 m (Figs. 4d–f). SoCal 2010 took place over 2 days in the Southern California Bight in much milder conditions. Winds ranged from 1 to  $9 \text{ m s}^{-1}$  with significant wave heights of 0.5 to 1.5 m (Figs. 4g–i).

Between the three experiments, 70 20-min records were analyzed with  $U_{10}$  of 1.6 to  $16 \text{ m s}^{-1}$ ,  $H_s$  of 0.7 to 4.7 m, and wave ages of  $c_m/u_* = 16$  to 150 (where  $c_m$  is defined in section 2c, and  $u_*$  is the friction velocity in the atmospheric boundary layer). Wind speed and wave age displayed a strong negative correlation during these experiments, reducing the available parameter space significantly.

### c. Wave field

The surface wave field was measured using the stereo video reconstructions of the surface described in SM15, combined with supporting laser wave-gauge data. Directional frequency spectra were calculated by creating a “synthetic wave-gauge array” with the stereo surface reconstructions. This consisted of five  $10 \text{ cm} \times 10 \text{ cm}$  patches on the reconstructed surface arranged with four patches in an approximately 1.5-m square and the fifth patch in the center. The average surface displacement over each small patch was recorded for each frame to produce a 20-Hz record of surface displacement at that location. Directional frequency spectra were calculated from these data using the iterative maximum likelihood method algorithm in the Wave Analysis for Fatigue and Oceanography (WAFO) MATLAB toolbox (Brodtkorb et al. 2000). Wavenumber spectra could not be computed directly from stereo reconstructions for scales larger than approximately 2 m, and so the directional frequency spectra were converted to wavenumber spectra using the

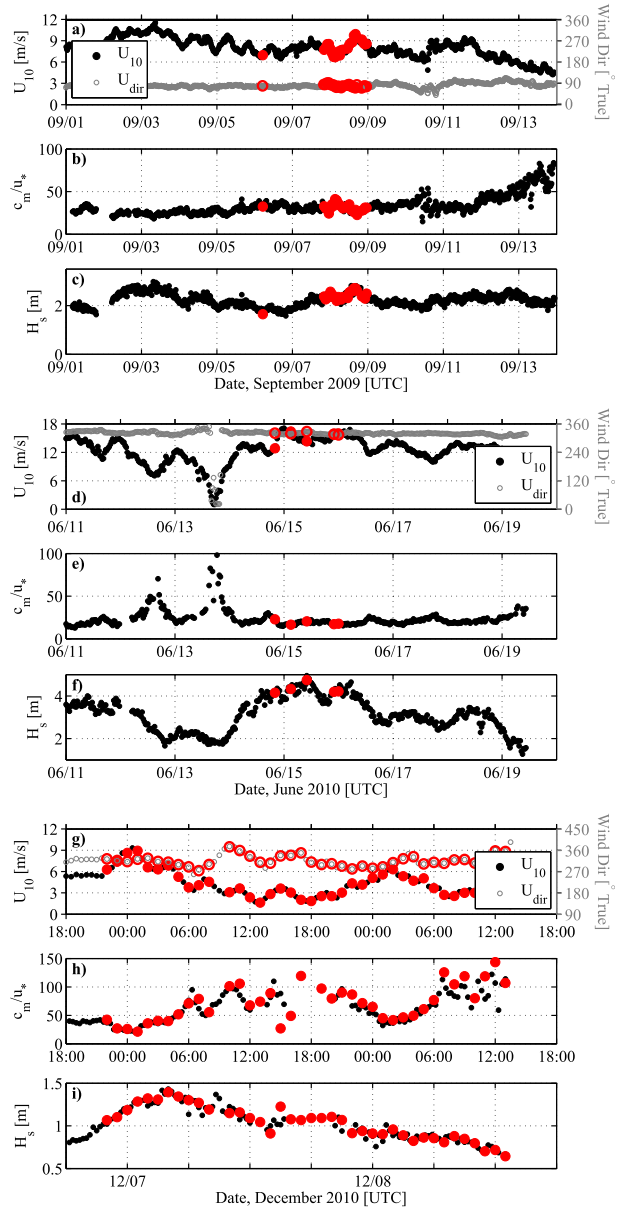


FIG. 4. The 20-min average wind and wave conditions during the three experiments used in this work. Red symbols indicate the data used for analysis. (a)–(c) RaDyO 2009, (d)–(f) HiRes 2010, and (g)–(i) SoCal 2010. (top) Wind speeds  $U_{10}$  shown as black circles and wind directions as gray circles. (middle) Wave age  $c_p/u_*$  and (bottom) significant wave height  $H_s$ . Note that the vertical and horizontal scales are different between the different experiments.

linear deep-water dispersion relation  $\omega^2 = gk$ , where  $\omega$  is the angular frequency of the waves,  $g = 9.81 \text{ m s}^{-2}$  is gravitational acceleration, and  $k$  is the wavenumber.

The mean wave speed  $c_m$  used here was an integral measure. The mean radian frequency  $\omega_m$  was defined using omnidirectional frequency spectra  $S_{\eta\eta}(\omega)$ :

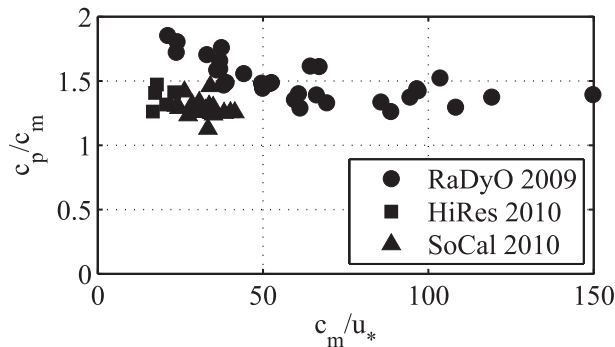


FIG. 5. Ratio of spectral peak wave phase speed  $c_p$  to spectral mean wave phase speed  $c_m$ .

$$\omega_m = \frac{\int_0^{\infty} \omega S_{\eta\eta}(\omega) d\omega}{\int_0^{\infty} S_{\eta\eta}(\omega) d\omega}. \quad (1)$$

The mean wave speed was then related to  $\omega_m$  using the linear deep-water dispersion relation  $c_m = g/\omega_m$ . This integral measure of spectral wave speed was chosen because of the multimodal spectra present during the field experiments;  $c_m$  was thought to be a better representative of the breaking waves than would be a simple spectral peak (often representative of swell). Figure 5 plots the phase speed of the spectral peak frequency  $c_p$ , divided by  $c_m$ , as a function of wave age  $c_m/u_*$ . The mean of  $c_p/c_m$  was found to be 1.45, with a weak dependence on wave age.

### 3. Dissipation by wave breaking

Wave breaking is expected to be an important source of near-surface turbulence, so a better understanding of near-surface turbulence requires a good understanding of the statistics of breaking. Phillips (1985) defined a distribution of breaker front length  $\Lambda(\mathbf{c})$  per unit area of sea surface per unit increment of breaking front velocity  $\mathbf{c} = (c, \theta)$  by  $\Lambda(\mathbf{c})$ , where  $c$  and  $\theta$  are the speed and direction of breaker front propagation, respectively.

Integrating  $\Lambda(\mathbf{c})$  azimuthally yields a distribution that is a function of speed only:

$$\Lambda(c) = \int_0^{2\pi} c \Lambda(c, \theta) d\theta. \quad (2)$$

The moments of  $\Lambda(\mathbf{c})$  have important physical interpretations. The fraction of surface area turned over by breaking fronts per unit time is the first moment of  $\Lambda(c)$  (Phillips 1985):

$$R = \int c \Lambda(c) dc, \quad (3)$$

which is related to heat and gas transfer between the ocean and the atmosphere.

The fifth moment of  $\Lambda(c)$  gives the total gravity wave energy dissipated by breaking waves per unit area of ocean surface:

$$F_{\text{br}} = \frac{\rho_w}{g} \int bc^5 \Lambda(c) dc, \quad (4)$$

where  $\rho_w$  is the water density. Phillips (1985) originally used a constant value for the “breaking parameter”  $b$ , but more recent work (e.g., Drazen et al. 2008; Romero et al. 2012) has shown that  $b$  varies over at least three orders of magnitude and depends on wave slope.

Figure 6 shows the measurements of  $\Lambda(c)$  given in Sutherland and Melville (2013) (for the same field experiments and sampling periods as in this work) as well as the first, fourth, and fifth moments. The fourth and fifth moments have been scaled by the spectral breaking parameter given by Romero et al. (2012):

$$b(k) = A_1 [B(k)^{1/2} - B_T^{1/2}]^{5/2}, \quad (5)$$

where  $B(k)$  is the azimuth-integrated saturation spectrum of the surface displacement,  $B_T$  and  $A_1$  are empirical constants, and  $k$  is mapped to  $c$  using the linear deep-water dispersion relation. This scaling makes the plotted fourth and fifth moments directly proportional to momentum flux from waves to currents (stress) and dissipation, respectively.

A central result of the Sutherland and Melville (2013) measurements was the extension of  $\Lambda(c)$  to include non-air-entraining microbreakers. They found the peaks of the  $\Lambda(c)$  distributions near the gravity-capillary phase speed transition  $c_{\text{gc}} = 23 \text{ cm s}^{-1}$ , indicating that microbreakers are far more prevalent than previous measurements observed. The high number of these microbreakers means that a significant fraction of dissipation and stress are supported by them. Figure 7 shows the cumulative integral of dissipation scaled by total dissipation, as a function of breaker crest speed  $c$ . The values of the curves at any  $c$  show the fraction of dissipation by breaking supported by breakers with speeds below that  $c$ . Making the conservative assumption that the approximate lower limit of air-entraining breakers is  $c = 2 \text{ m s}^{-1}$ , as indicated by the vertical gray dashed line in Fig. 7 (cf. Fig. 6 below, and Fig. 3 of Sutherland and Melville 2013), dissipation by microbreakers accounts for between 20% and 90% of total dissipation by breaking. Microbreakers account for a larger fraction of total dissipation during the old wave age, light wind conditions than they do for the younger waves in strong winds.

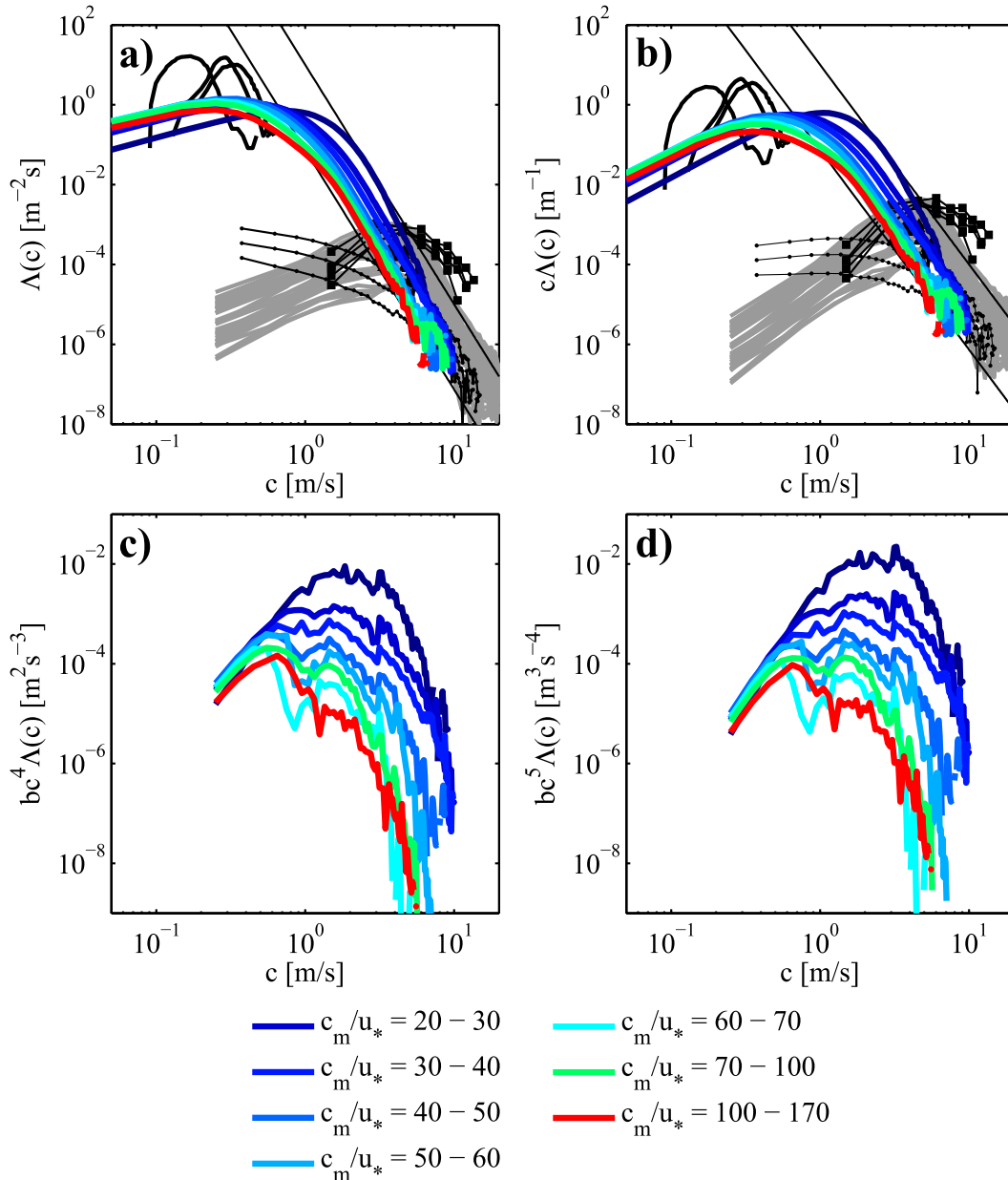


FIG. 6. Moments of  $\Lambda(c)$ : (a) zeroth, (b) first, (c) fourth, and (d) fifth. The fourth and fifth moments have been multiplied by the dimensionless breaking parameter  $b$ , making them directly proportional to stress and dissipation, respectively. Here the breaking parameter  $b = b(k)$ , is obtained by following Eq. (5), and  $k$  is mapped to  $c$  using the linear deep-water dispersion relation. Colored lines are data from all three experiments, analyzed as in Sutherland and Melville (2013) and binned by wave age. In (a) and (b), data from the literature are shown for comparison; thick black lines are from the laboratory measurements of Jessup and Phadnis (2005). Field measurements are from the following: Melville and Matusov (2002), lines with small dots; Gemmrich et al. (2008), lines with squares; and Kleiss and Melville (2010), solid gray lines. The thin straight black lines are  $c^{-6}$ .

The relatively small amplitude of these microbreakers suggests that their large contribution to near-surface TKE dissipation is likely to be concentrated in a thin layer near the surface. Phase speeds of  $c = 2 \text{ m s}^{-1}$  correspond to wavelengths of approximately 2.5 m. Using typical slopes at breaking,  $ak = 0.3$  (Romero et al. 2012), would correspond to breaking waves of amplitude

$a = O(10) \text{ cm}$ . Rapp and Melville (1990) showed that the turbulence associated with breaking rapidly penetrates to a depth comparable to the wave amplitude (see also Melville et al. 2002). This implies, in the absence of other mechanisms, between 20% and 90% of dissipation by breaking occurs within approximately  $O(10) \text{ cm}$  of the sea surface.

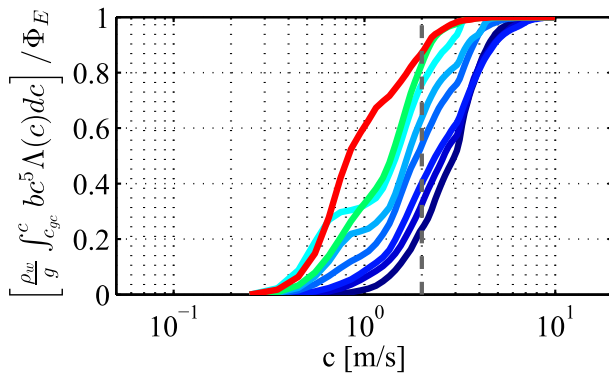


FIG. 7. Cumulative integral of dissipation normalized by total dissipation and plotted as a function of breaker crest speed  $c$ . This shows the fraction of energy dissipated by breakers with crest speeds below any  $c$ . Curves have been binned by wave age, and the color of the curves indicates that wave age (using the same color scale as Fig. 6). Total dissipation by breaking  $F_{br}$  is defined in Eq. (4). The vertical dashed gray line indicates the approximate lower speed limit of air-entraining breakers.

This simplistic view is complicated by the advection of near-surface turbulence (from small wave breaking) downward by larger breakers and other vertical transport processes like Langmuir circulations. The LES simulations of Sullivan et al. (2007) included the effects of these processes advecting turbulence, but because the breaker statistics that they used did not include the high level of microbreaking observed by Sutherland and Melville (2013), their simulations likely underestimated this shallow dissipation layer and the vertical transport of this turbulence by the larger-scale Langmuir turbulence.

#### 4. Surface TKE dissipation

SM15 describe a new technique for measuring surface TKE dissipation that was developed for the analysis of these experiments. In that work, the surface velocity fields measured using the stereo IR imagery were separated, using a Helmholtz decomposition, into irrotational wave and rotational turbulence components. TKE dissipation was calculated by either fitting wavenumber spectra of rotational surface velocities to the Kolmogorov inertial subrange or by using an analogous technique to fit the measured spectrum of vertical vorticity to a universal spectrum. Results from the different techniques were consistent. For this work, surface TKE was measured using the vorticity spectral fit method, and because of the observed dependence of subsurface TKE dissipation on depth (also found by Gemmrich 2010), the assumption of 2D turbulence was used. Individual dissipation measurements represent averages over an approximately  $2\text{ m} \times 2\text{ m}$  patch of ocean surface over a time period

of 0.05 s for each pair of image frames. These individual measurements were then sampled at 4 Hz for each 20-min period analyzed.

#### 5. Subsurface turbulence

Subsurface turbulence was measured using the LTMI array and Aquadopp floats.

Subsurface dissipation was calculated using the method of structure functions described by Wiles et al. (2006), as implemented by Thomson (2012). The “one-sided” structure function can be defined by

$$D(x, r) = \langle [u'(x) - u'(x - r)]^2 \rangle, \quad (6)$$

where  $u'(x)$  is the fluctuating velocity in the positive  $x$  direction (away from the instrument in all beams, toward the surface in the vertical beam),  $r$  is the separation of measurements, and the angle brackets denote an average in time. Kolmogorov (1991) showed that, at scales much larger than the scale of dissipation, the structure function can be written in terms of dissipation:

$$D(z, r) = C_v^2 \varepsilon^{2/3} r^{2/3}. \quad (7)$$

The term  $C_v$  is a universal constant; the value used here  $C_v^2 = 2.1$  is from Wiles et al. (2006). Equation (7) is the direct spatial analog of the better-known  $k^{-5/3}$  inertial subrange wavenumber spectrum. Wiles et al. (2006) fit a curve of the form

$$D(z, r) = N + Ar^{2/3} \quad (8)$$

to the measured structure function, where  $A = C_v^2 \varepsilon^{2/3}$ ,  $N = 2\sigma_N^2$ , and  $\sigma_N$  is the standard deviation of the noise in the system.

Then assuming that  $N \ll Ar^{2/3}$ , as in Gemmrich (2010),

$$\varepsilon \approx \left( \frac{A}{C_v^2} \right)^{3/2}, \quad (9)$$

which can be considered an upper bound on dissipation because the noise is included in the measurement of dissipation.

Dissipation was calculated in this manner using along-beam velocities for each of the three Aquadopp beams. However, before dissipation could be calculated, significant processing was required. This included phase unwrapping, data quality control, transforming to surface-relative coordinates, structure function calculation, and structure function temporal averaging. The processing sequence is described in detail in appendix A.

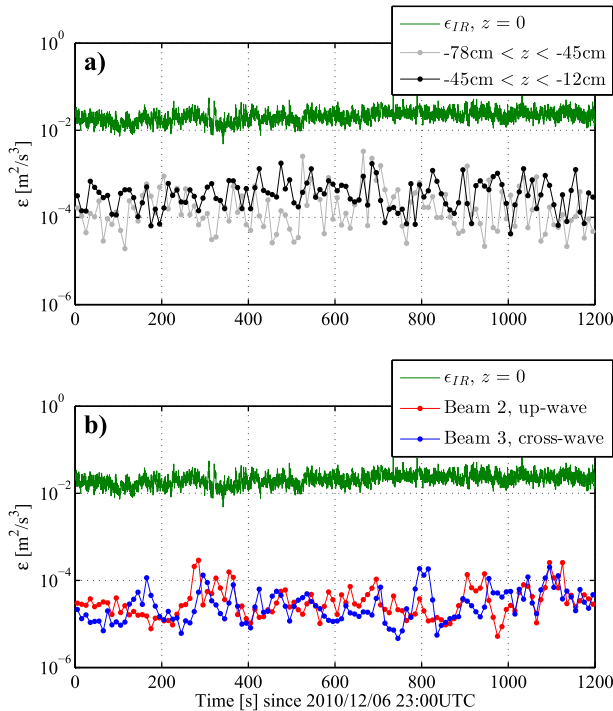


FIG. 8. Near-surface TKE dissipation. Data in green are from the stereo IR PIV measurements. Lines with dots are from the subsurface measurements, each dot corresponding to a 10-s average. (a) Dissipation measured using the vertical beam of the near-surface Aquadopp, averaged between 12 and 45 cm from the instantaneous surface (black) and between 45 and 72 cm from the surface (gray). (b) Dissipation measured using the horizontal beams in the upwave (red) and across-wave (blue) directions. The mean depth of the horizontal beams was 1.05 m and the section of each horizontal beam used for dissipation calculation was a distance of 0.5 to 1.2 m from the instrument head.

The final results of this processing are records of dissipation with a spatial resolution of  $r_{\max} = 0.12$  m and a temporal resolution of 10 s. Figure 8 shows example time series of dissipation calculated using the uppermost Aquadopp. An example dissipation profile from the LTMI array, using the same near-surface data as in Fig. 8, is shown in Fig. 9. In this case the average dissipation values are roughly monotonic with depth, but the spread of data exceeds two orders of magnitude.

As noted in the introduction, accidental capture of turbulent wakes is always a concern when making measurements of this kind. In addition to the original wake-minimizing design for the LTMIs, several steps were taken to minimize wake effects.

First, in order to avoid sampling the wake of *FLIP*'s hull, mean currents were checked for each sampling period and at each instrument depth level. Whenever an instrument was downstream of either another instrument or *FLIP*'s hull, that 20-min record was removed. During the SoCal 2010 experiment, this resulted in the removal

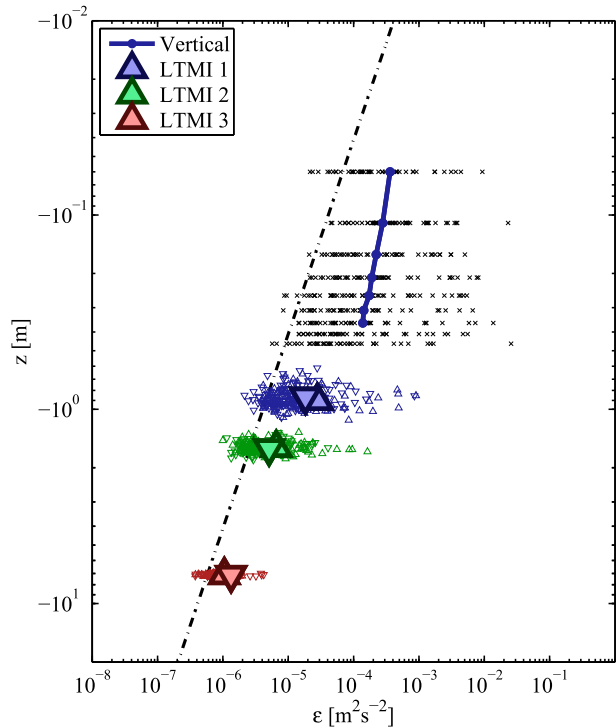


FIG. 9. Subsurface dissipation during SoCal 2010 measured by the LTMI array over 20-min starting 2300 UTC 6 Dec 2010, compared with wall layer scaling (dashed-dotted line). The wall layer  $\epsilon_{wl}(z)$  was computed with Eq. (11). Colors correspond to LTMI number; one is blue, two is green, and three is red. The thick blue line is the 20-min average profile from the upward beam on LTMI1, and the small black crosses are individual 10-s samples from the same beam of LTMI1. The large triangles are 20-min averages from the horizontal beams of the LTMIs; upward triangles are from the upcurrent beam (beam two), and downward triangles are from the cross-current beam (beam three). Small triangles correspond to 10-s averages. All depths are relative to the instantaneous surface.

of 8 out of 39 records for LTMI1, 15 out of 39 for LTMI2, and 18 out of 39 for LTMI3. Because of more steady conditions, no record removal was required during RaDyO 2009 or HiRes 2010.

During the SoCal 2010 experiment, standard deviations of velocities were typically higher than the mean velocities, particularly for the near-surface LTMI1. This means that instrument wake can be expected to be readvected through at least part of the sample volume (see appendix B). Since the Aquadopp has an approximately 1-m beam length, it was possible to utilize only the outer portion of the beam for computing dissipation. In the case of the horizontal beams, the near-instrument blanking distance was determined by finding the region near the end of each beam where time-mean dissipation levels remained constant as a function of distance from the instrument.

Figure 10 shows all 20-min average subsurface dissipation measurements available. Trends of increasing

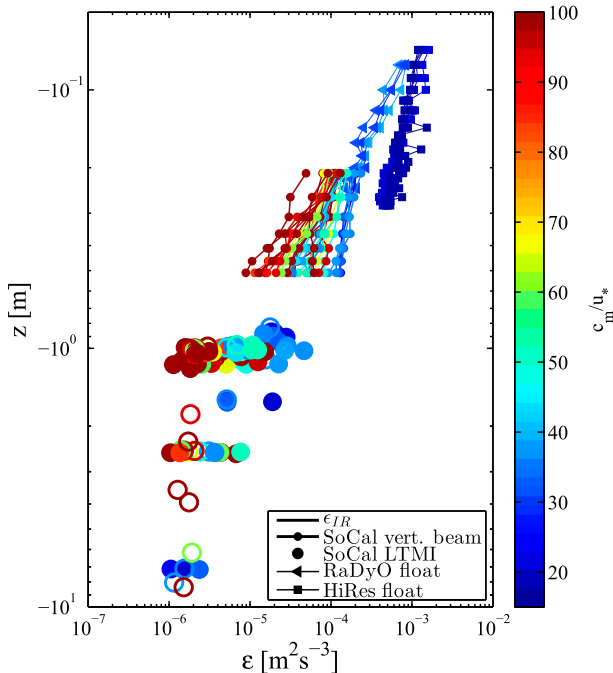


FIG. 10. All available 20-min average subsurface dissipation profile measurements. The lines with dots are from the upward-looking beam of the near-surface LTMi during SoCal 2010 and are relative to the instantaneous surface. Large circles are from the horizontal beams of the LTMis during SoCal 2010, filled circles are from increasing or constant wind conditions, and hollow circles are from decreasing wind conditions. Lines with squares are from the Aquadopp float during HiRes 2010. Lines with triangles are from the Aquadopp float during RaDyO 2009. Color corresponds to wave age.

dissipation with decreasing wave age are observed as expected, as is an increase of dissipation near the surface. The form of these profiles will be examined in section 6.

The lower and upper limits of the data, at approximately  $\varepsilon = 10^{-6} \text{ m}^2 \text{ s}^{-3}$  and  $\varepsilon = 10^{-3} \text{ m}^2 \text{ s}^{-3}$ , respectively, are the result of instrument limitations. The lower limit is set by the noise level of the Aquadopp in the experimental conditions. The upper limit is partially set by velocity phase wrapping within the instrument, making it unlikely that the true velocity gradients (needed for an accurate structure function) were determined beyond a certain level. Despite these limitations, these measurements have still managed to achieve approximately three decades of dynamic range. This resolves most of the dissipation profiles over the depths within approximately one significant wave height ( $H_s$ ) of the surface.

## 6. Discussion

One of the most cited studies of elevated TKE dissipation near the surface is the work of T96 and D96. They

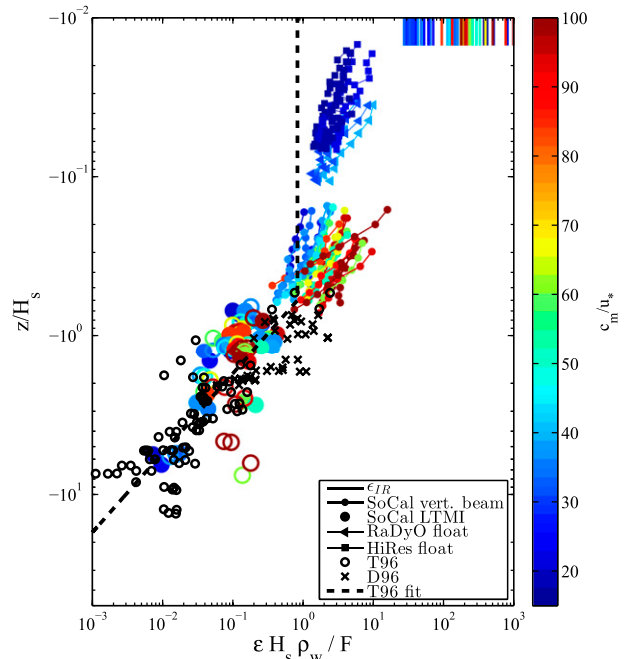


FIG. 11. Subsurface TKE dissipation scaled by energy flux  $F$  (discussed in appendix C) and significant wave height  $H_s$  as in T96. Our data were scaled using  $F = F_{ds}$  (see appendix C), whereas the data from T96 and D96 were scaled using  $F = F_{TD}$  (see appendix C). Color corresponds to wave age, and each line or symbol represents a 20-min average. Short solid lines are the surface IR measurements extended downward to an arbitrary height for visibility in this logarithmic plot. From SoCal 2010, lines with dots are from the vertical beam of the near-surface Aquadopp, circles are from the LTMi horizontal beams, solid circles indicate periods with rising or constant winds, and empty circles indicate periods with falling winds. From RaDyO 2009, the lines with left triangles are from the Aquadopp float. The data from the Aquadopp float during HiRes 2010 are the lines with squares. The black symbols are the data of T96 (o) and D96 (x); the thick dashed black line indicates the best fit given by T96,  $\varepsilon H_s F / \rho_w = 0.3(z/H_s)^{-2}$ , including their expected constant near-surface dissipation layer.

found dissipation levels exceeded those predicted by a wall layer at depths shallower than approximately 10 significant wave heights  $H_s$ . More specifically, T96 fit their data to a curve of the form

$$\frac{\varepsilon H_s \rho_w}{F_{TD}} = 0.3 \left( \frac{z}{H_s} \right)^{-2}, \quad (10)$$

where  $F_{TD}$  was the wind input (see appendix C) and  $z$  was relative to the mean sea surface. At greater depths, they hypothesized a return to a wall layer decay. Near the surface, above  $0.6H_s$ , they expected a layer of constant dissipation. That depth was set so that the integrated water column dissipation would equal the energy input of the wind.

In this work, elevated turbulence near the surface was also found. Figure 11 shows the subsurface data taken here scaled by energy flux as in T96. Instead of using the wind input function used by T96 and D96,  $F_{TD}$ , dissipation was scaled by wave dissipation  $F_{ds}$  (see appendix C). The decision to use  $F_{ds}$ , rather than  $F_{TD}$ , was made because  $F_{ds}$  is expected to be a more accurate measure of energy lost by the wave field at the relatively high wave ages of these experiments. At lower wave ages, in the  $c_p/u_* = 13 - 29$  range used by D96,  $F_{TD}$  approaches  $F_{ds}$  (see Fig. C1). Another important note when comparing these data with those of D96 in Fig. 11 is that here measurements have been made in coordinates relative to the instantaneous surface, whereas D96's were relative to the mean surface.

In the depth range where D96 had data,  $|z|/H_s > 0.6$ , the measured dissipation profiles from our work roughly follow the  $z^{-2}$  shape found by D96 [Eq. (10)]. However, the scatter is significant, and our measurements appear to be lower than theirs, at least at depths  $O(H_s)$ . This is most likely because of the differing reference frames of the two sets of measurements. Above  $0.6H_s$ , where T96 and D96 expected a layer of constant dissipation, our results show  $z^{-1}$  profiles. This does not contradict the measurements of T96 and D96, since they did not sample this region.

More recent studies have not found the layer of constant dissipation expected by T96 and D96. Work by Gemmrich (2010) observed a dissipation profile that followed a  $z^{-1}$  curve from the deepest measurements, approximately  $2H_s$ , up to approximately  $0.3H_s$ , where dissipation was enhanced beyond the  $z^{-1}$  curve. However, his dissipation in the  $z^{-1}$  region was not the classic wall layer

$$\varepsilon_{wl}(z) = \frac{u_{*w}^3}{\kappa z}, \tag{11}$$

where  $u_{*w}$  is the friction velocity in the water, and  $\kappa = 0.4$  is the von Kármán constant. Instead, an enhancement of dissipation over the wall layer  $\varepsilon/\varepsilon_{wl}$  by a factor of between 5 and 20 was observed. Gemmrich found that  $\varepsilon/\varepsilon_{wl}$  was greatest for lower wind speeds and least for higher wind speeds. In our measurements, an enhancement over wall layer values was also observed. A trend of increased enhancement over the wall layer with increased wave age was found. Figure 12 shows the observed subsurface data binned by wave age (in this case, defined as  $c_p/U_{10}$ , in contrast to the  $c_m/u_*$  used in the rest of the paper) and scaled by  $\varepsilon_{wl}$ . In the near-surface region, dissipation profiles showed a  $z^{-1}$  dependence, with levels exceeding wall layer levels by a factor of approximately 5 in the lowest wave age conditions and 3000 in the highest

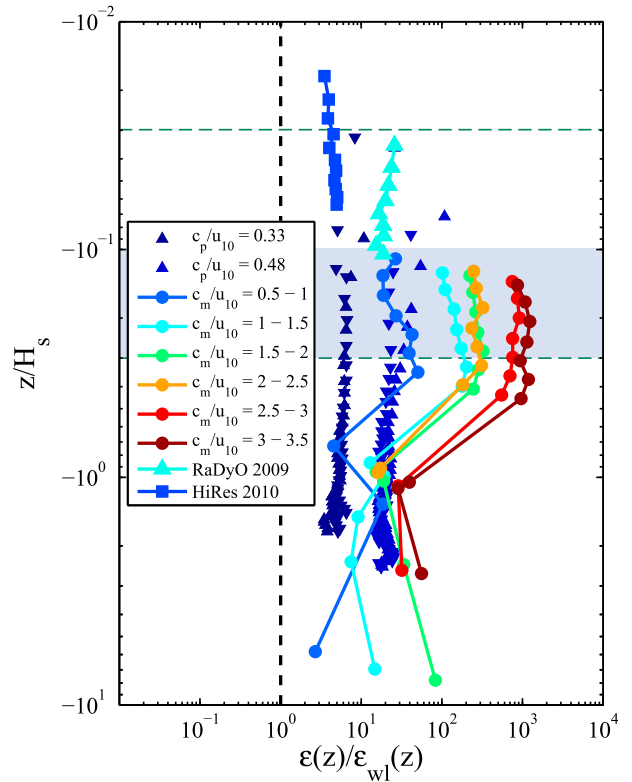


FIG. 12. Subsurface TKE dissipation, bin averaged by color-coded wave age and scaled by wall layer values  $\varepsilon_{wl}(z)$ . The unconnected triangles are from Gemmrich (2010), the connected triangles are from RaDyO 2009, the connected squares are from HiRes 2010, and the connected circles are from SoCal 2010. Note the trend toward increased  $\varepsilon(z)/\varepsilon_{wl}(z)$  with increased wave age. The shaded region indicates the range of depths  $-z/H_s = 0.1-0.3$ , over which  $\varepsilon(z)/\varepsilon_{wl}(z)$  for the SoCal 2010 and Gemmrich (2010) data were averaged in Fig. 13. The horizontal dashed lines indicate the depth range  $-z/H_s = 0.03-0.3$ , over which the RaDyO 2009 and HiRes 2010 data were averaged in Fig. 13. The vertical black dashed line indicates classical wall layer dissipation  $\varepsilon(z)/\varepsilon_{wl}(z)$ .

wave age conditions. Below a depth of approximately  $z/H_s = 0.5$ , scaled dissipation  $\varepsilon(z)/\varepsilon_{wl}(z)$  decreased with increasing depth, as the dissipation profile presumably tended toward the true wall layer.

Elevation of dissipation above wall layer levels  $\varepsilon(z)/\varepsilon_{wl}(z)$ , averaged over the depth range where dissipation showed a  $z^{-1}$  profile, is plotted in Fig. 13. The averaging depth ranges were  $z/H_s = 0.1 - 0.3$  for the data from SoCal 2010 and Gemmrich (2010) (indicated by the shaded region in Fig. 12), and  $z/H_s = 0.03 - 0.3$  for data from HiRes 2010 and RaDyO 2009 (horizontal dashed lines in Fig. 12). Data from RaDyO 2009 and HiRes 2010 were averaged to shallower scaled depths because, due to large waves, their measurements were mostly above  $z/H_s = 0.1$ . The elevation of dissipation over a wall layer for our data has a dependence on  $c_p/U_{10}$ , where

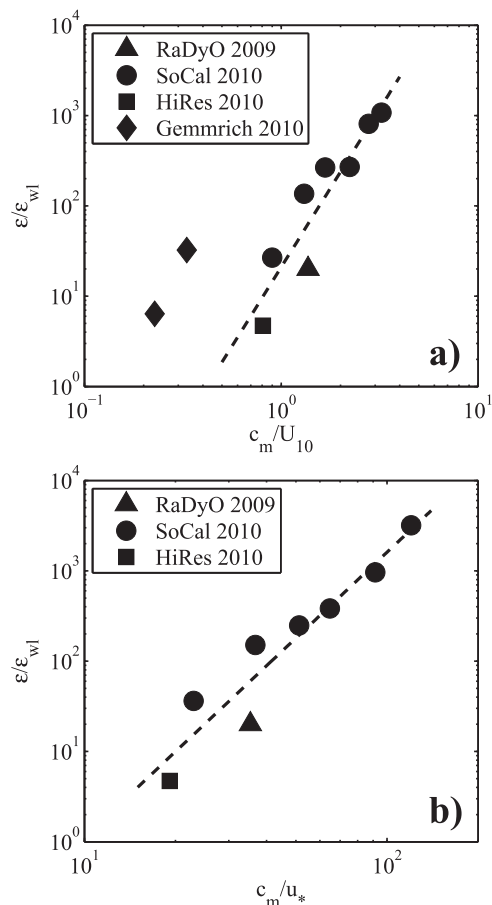


FIG. 13. Elevation of TKE dissipation above classical wall layer values, plotted as a function of wave age. Triangles, circles, and squares are from our work, diamonds are from Gemmrich (2010). The value  $\varepsilon(z)/\varepsilon_{wl}(z)$  has been averaged over the depth range  $-z/H_s = 0.1\text{--}0.3$  (shaded region in Fig. 12) for the SoCal 2010 and Gemmrich (2010) data, and  $-z/H_s = 0.03\text{--}0.3$  (horizontal dashed lines in Fig. 12) for the RaDyO 2009 and HiRes 2010 data. Data from RaDyO 2009 and HiRes 2010 were averaged to shallower scaled depths because, due to large waves, their measurements were mostly above  $z/H_s = 0.1$ . (a) Uses wave age computed as  $c_m/U_{10}$ . The dashed line is a fit to our data, where  $\varepsilon/\varepsilon_{wl} = 21(c_m/U_{10})^{3.5}$ . The Gemmrich (2010) measured  $c_p$  has been converted to  $c_m$  using the mean relationship from our measurements,  $c_p/c_m = 1.45$  (noted in section 2c). (b) Wave age has been computed as  $c_m/u_*$ , and the fit to our data is then  $\varepsilon/\varepsilon_{wl} = 7.8 \times 10^{-4}(c_m/u_*)^{3.15}$ .

$$\varepsilon/\varepsilon_{wl} = 21 \left( \frac{c_p}{U_{10}} \right)^{3.5}. \quad (12)$$

The Gemmrich (2010) data show a similar power dependence but are at a higher level than ours. This suggests that, not surprisingly,  $c_p/U_{10}$  is not a sufficient parameter for describing near-surface turbulence, at least across the widely differing conditions found in this work versus those experienced by Gemmrich (2010).

Another view of dissipation near the surface is provided by the LES of Sullivan et al. (2004, 2007). They modeled individual breaking waves as body forces applied to the fluid. The body forces were based on the laboratory measurements of Rapp and Melville (1990) and Melville et al. (2002). They then used an ensemble of those breakers, with breaker crest length distributions matching those of Melville and Matusov (2002), to investigate their impacts on the dynamics of the upper ocean. Figure 14 shows a comparison of their modeled dissipation profile with the results found here. It can be seen that there is general agreement, but our measurements are lower at depth and higher near the surface. As noted in section 3, the breaking statistics used by Sullivan et al. (2007) underestimated the number of small breakers at low speeds. This means that the LES would have applied too much energy to large breakers capable of injecting turbulence deep into the water column and underestimated near-surface dissipation—consistent with the comparison shown. It would be very interesting to see a revisit of these LES simulations with higher vertical resolution near the surface and using the updated low-speed breaking statistics of Sutherland and Melville (2013).

So far, with caveats regarding reference frames, the T96 scaling appears to be not inconsistent with our observations for depths greater than one significant wave height from the sea surface. Closer to the surface, a  $z^{-1}$  profile seems more appropriate, although there is significant spread in the data. The true uncertainty lies in the very near-surface region, in the top few centimeters of the ocean. As noted in section 3, dissipation of between 20% and 90% of the total dissipation by breaking is expected to occur within  $O(10)$  cm of the sea surface. Understanding this surface layer was a major motivation for using IR imagery to measure dissipation at the surface.

#### a. Integrated dissipation

The goal with these combined surface and subsurface measurements is to be able to constrain the energy budget in the near-surface boundary layer.

To integrate the total subsurface TKE dissipation, stereo IR and LTMI measurements were combined. Starting at the surface, a layer of constant dissipation  $\varepsilon(z) = \varepsilon_s$  was assumed from the surface to a depth  $z_s$ . This layer was connected to the subsurface layer by a  $\varepsilon(z) = az^{-1}$  decay, where  $a$  was determined by matching dissipation at the top level of the subsurface measurements. The term  $z_s$  was then taken to be the depth at which  $\varepsilon_s = az_s^{-1}$ . Figure 15 shows a schematic of this extrapolation technique. The  $z^{-1}$  dependence was chosen because near-surface measurements in this work showed a  $z^{-1}$  depth dependence as close to the surface as it was possible to measure from

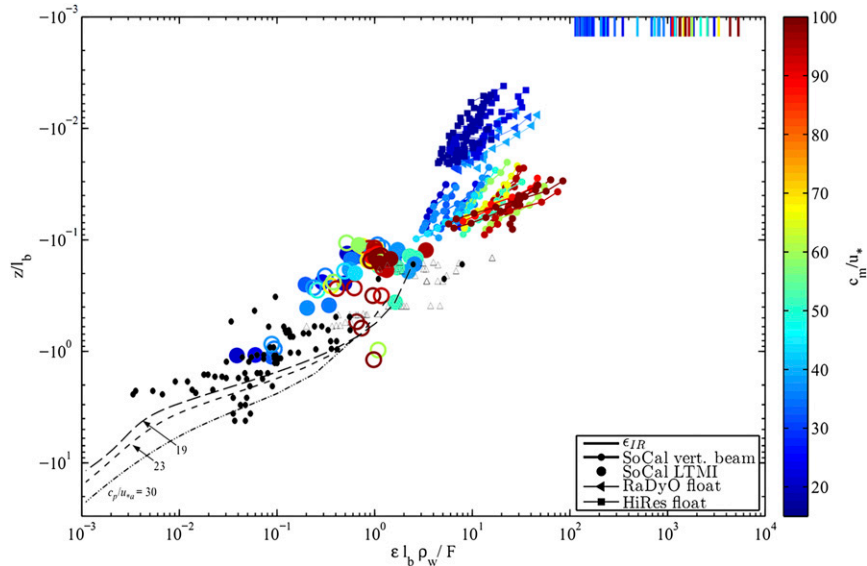


FIG. 14. TKE dissipation scaled by energy flux  $F$  (defined in appendix C) and length scale  $l_b$ , as in Sullivan et al. (2007). For the measurements  $l_b = c_p^2/g$  and for the LES  $l_b = c_E^2/g$ , where  $c_E$  is the phase speed of the peak in the breaker energy flux spectrum. Energy flux definitions are included in appendix C. In this figure, our data were scaled by wave dissipation  $F = F_{ds}$ , whereas the data from T96 and D96 were scaled by wind input  $F = F_{TD}$ . The dashed lines indicate the Sullivan et al. (2007) LES results for three different wave ages. In our data, color corresponds to wave age and each line or symbol represents a 20-min average. Short solid lines are the surface IR measurements extended downward to an arbitrary depth in order to make them visible in this logarithmic plot. From SoCal 2010, lines with dots are from the vertical beam of the near-surface Aquadopp, circles are from the LTMI horizontal beams, solid circles indicate periods with rising or constant winds, and empty circles indicate periods with falling winds. From RaDyO 2009, the lines with left triangles are from the Aquadopp float. The data from the Aquadopp float during HiRes 2010 are the lines with squares. The black symbols are the data of T96 (dots) and D96 (triangles).

below. Linear interpolation was used between all LTMI depth levels. Below the bottom LTMI, a  $z^{-2}$  profile that intersected the LTMI dissipation value was assumed. The dissipation profile was integrated from the surface to a depth of 20 m. Integration was found to be insensitive to the lower depth limit chosen.

Figure 16 shows a comparison of integrated subsurface TKE dissipation compared with dissipation from breaking calculated by Sutherland and Melville (2013). The abscissa in this plot corresponds to the ordinate in Fig. 5a of Sutherland and Melville (2013). A large uncertainty in the subsurface measurements is the shape of the profile connecting the surface IR measurements to the subsurface measurements. In Fig. 16, the profile chosen was an extrapolation of the observed  $z^{-1}$  profile. However, since we do not have subsurface measurements extending between the surface and approximately 6–12-cm depth (depending on the experiment), the actual profile shape is not known. To explore the sensitivity of this extrapolation, it is useful to

examine the limiting cases. If the gradient of dissipation with respect to depth near the surface does not change sign, then the maximum and minimum integrated dissipation values are indicated by the upper and lower error bars in Fig. 16. The uncertainties range between a factor of 2 and an order of magnitude, highlighting the critical importance of dissipation in the top few centimeters of the ocean.

Agreement between subsurface TKE dissipation and dissipation by breaking is good for wave ages below approximately  $c_m/u_* = 50$ , corresponding to wind speeds above  $4 \text{ m s}^{-1}$  (because of the strong negative correlation between wind speed and wave age). This agreement covers the range of approximately  $0.1\text{--}2 \text{ W m}^{-2}$  and indicates that breaking is the dominant source of turbulence in wave-affected surface layers under those conditions.

The comparison between our integrated dissipation values and those from the literature is informative. For example, as noted above, the well-cited work of D96 assumed a constant layer of dissipation from the surface to

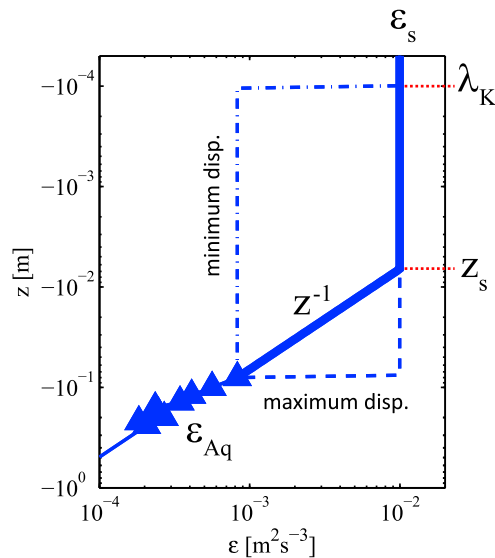


FIG. 15. Technique for extrapolating from subsurface to surface data. The observed  $z^{-1}$  profile of the Aquadopp data  $\varepsilon_{\text{Aq}}(z)$  is extended upward until it reaches the measured surface dissipation  $\varepsilon_s$  (thick blue line). The limits on this extrapolation, assuming that the derivative of the dissipation profile does not change sign, are indicated by the thin dashed lines. The lower limit assumes that dissipation remains constant from the depth of the Aquadopp measurements up to a depth of  $\lambda_K$  (the Kolmogorov scale of the surface turbulence) and then is the surface value up to the surface (dashed-dotted line). The upper limit assumes that dissipation is a constant value of  $\varepsilon_s$  for all depths above the depth of the Aquadopp (dashed line). These limits are indicated as the error bars of vertically integrated dissipation in Fig. 16.

a depth of  $0.6H_s$  in order to balance integrated subsurface dissipation with wind input. In contrast, our work shows strongly increasing TKE dissipation in this same near-surface depth range, while also showing a deeper dissipation profile similar to the one observed by D96. When comparing the D96 dissipation profiles with ours, two things become apparent.

First, although our measurements in the depth range of approximately  $2H_s < H_s < 0.6H_s$  lie within the scatter of the measurements of D96 at those depths, the D96 measurements appear to be biased high compared to ours. This bias is likely because their measurements were taken in a reference frame relative to the mean surface rather than the instantaneous surface, as ours were. It should also be noted that the scatter of data is also large, well exceeding an order of magnitude.

Second, the D96 measurements were all made during conditions where the relative importance of the near-surface microbreaking would be expected to be minimal. Section 3 describes the relative importance of microbreaking as a function of wave age. D96 had wave ages of  $c_p/u_* = 15 - 30$ ; in those conditions, Fig. 7 shows that

dissipation by microbreaking would be expected to account for only approximately 20% of total energy dissipation.

Another example of measurements of near-surface dissipation profiles, this time supported by concurrent whitecap measurements, is the work of Schwendeman et al. (2014). Their apparatus consisted of an autonomous float equipped with an upward-looking Aquadopp for turbulence measurements and a downward-looking video camera to capture whitecaps.

Their near-surface dissipation measurements were taken from a few centimeters below the sea surface down to a depth of 0.6 m, capturing much of the near-surface layer. Using those measurements (and making some assumptions about background turbulence levels), they were able to balance modeled wave field dissipation with integrated subsurface dissipation.

The whitecap measurements of Schwendeman et al. (2014) did not capture microbreaking but were used to measure the breaker crest length distribution  $\Lambda(c)$ . Unfortunately, they did not directly compute dissipation by breaking as in Eq. (4), using a spectral breaking parameter defined as in Eq. (5). Instead, they equated integrated subsurface dissipation to Eq. (4) and solved for a constant breaking parameter  $b$ . In any event, the high wind and low wave age conditions of their study would have minimized the contribution of microbreaking to total dissipation.

These examples highlight that, despite the fact that dissipation by microbreakers can account for between 20% and 90% of total wave dissipation, the contribution by microbreaking is still within the uncertainty of past studies.

### b. Other sources of turbulence

In addition to wave breaking, other sources of turbulence are present near the sea surface, and it is expected that in some conditions, those sources may become significant. Although for wave ages below approximately  $c_m/u_* = 50$ , dissipation by breaking is well matched by integrated subsurface dissipation, at older wave ages (and lighter winds), measured TKE dissipation is well above levels expected due to wave breaking alone.

Because of the high wave ages present, the possibility that this additional turbulence was due to the dissipation of swell energy was considered. However, the observed TKE dissipation was two to three orders of magnitude larger than the dissipation rate of swell energy expected [based on the observations of Ardhuin et al. (2009)].

Other potential nonbreaking contributors to the background turbulence include convection, Langmuir circulations, breaking internal waves, and shear production. Recent work by Grant and Belcher (2009) and Belcher et al. (2012) has focused on the relative importance of turbulence due to shear production, Langmuir

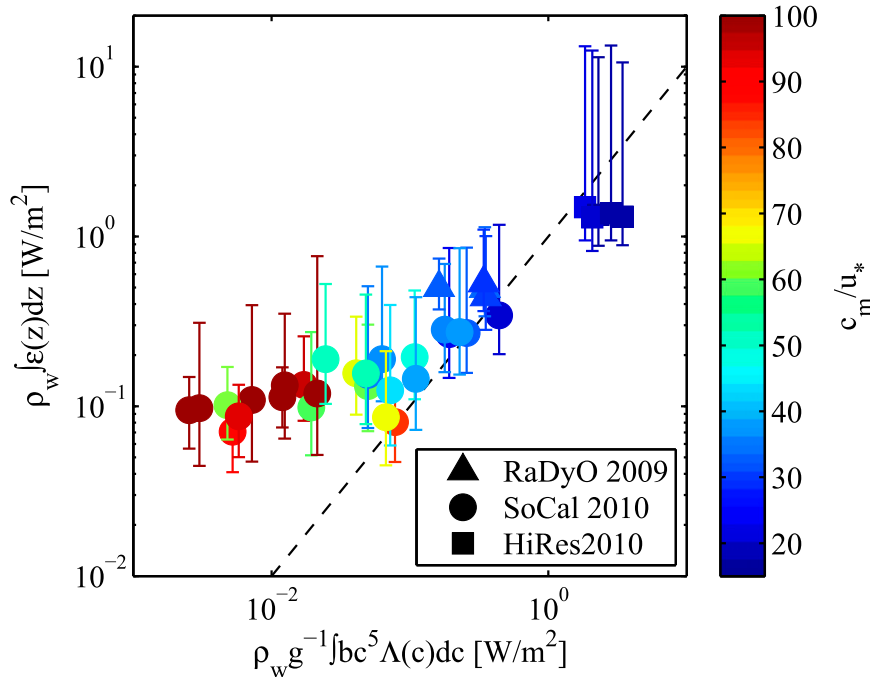


FIG. 16. Integrated water column dissipation compared with energy dissipation by wave breaking, measured using the integrated fifth moment of  $\Lambda(c)$ . Subsurface measurements have been connected to surface measurements using a  $z^{-1}$  profile. Triangles and squares are from RaDyO 2009 and HiRes 2010, respectively; for these data, the only underwater data available were from the Aquadopp float. Circles are from SoCal 2010, where underwater measurements were from the LTMI array. Coloring is by wave age. Error bars indicate the maximum uncertainty in the integrated dissipation due to the extrapolation between the subsurface and surface measurements (Fig. 15). The dashed line is a 1:1 match.

circulations, and convection. Belcher et al. (2012) found that over large areas of the ocean, Langmuir turbulence is likely a dominant mechanism for dissipation. Their results were supported by the field measurements of Sutherland et al. (2014). Following the criterion set forth by Belcher et al. (2012), it was possible to categorize each of the 20-min averaging periods sampled here. Langmuir turbulence was expected to be dominant over turbulence from wind shear in all cases, and in all but three light wind cases Langmuir turbulence was expected to be stronger than convection. Langmuir turbulence could not, however, account for the very high levels of near-surface TKE dissipation.

c. Sampling an intermittent process

Figure 8 shows time series of dissipation at and near the surface. Immediately obvious is the relatively constant value of surface dissipation compared to the subsurface. A combination of factors contributes to this. First, the surface measurements were a spatial average over a much larger area than the subsurface measurements. The surface measurements covered an approximately  $2\text{ m} \times 3\text{ m}$  patch of the ocean. The horizontal sampling regions of the

subsurface measurements were much smaller; the cross section of the vertical Aquadopp beams was a maximum of approximately  $3\text{ cm} \times 3\text{ cm}$ , and the horizontal beams were approximately  $3\text{ cm} \times 100\text{ cm}$ .

Second, as discussed in section 3, a large fraction of dissipation by breaking is supported by small breaking waves. The integrated first moment of  $\Lambda(c)$  (Fig. 6) gives the fraction of surface area overturned by breaking waves per unit time. This fractional overturn is one to two orders of magnitude larger for microbreakers than for larger air-entraining breakers. In the case of the time series in question, this means that any given point would see an average of one microbreaker pass every 1.4 s, whereas it would only see an average of one air-entraining breaker pass every 80 s. Breakers inject turbulence to depths comparable to their height, so the deeper the instrument, the more intermittent its breaker-driven turbulence will become.

The explanation for the behavior of the dissipation time series in Fig. 8 is then clear. The IR cameras spatially average extremely frequent microbreakers, whereas the deep horizontal Aquadopp beams may only sample the much more intermittent large breakers or turbulence

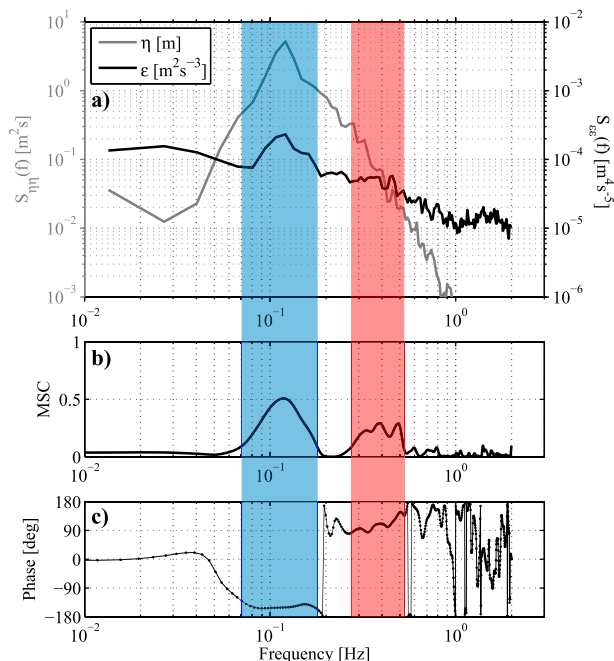


FIG. 17. Coherence of surface displacement and dissipation from IR imagery. (a) Frequency spectra of surface displacement  $\eta$  (m) and dissipation  $\varepsilon$ , ( $\text{m}^2 \text{s}^{-3}$ ). (b) Magnitude squared coherence between dissipation and displacement. (c) Phase of wave dissipation coherence. Angles are defined such that at  $90^\circ$ , the dissipation lags the wave peak by  $90^\circ$ . The highlighted regions indicate the frequency bands to which the wave signal was filtered for computation of the wave-phase averages of dissipation shown in Fig. 18. The red band corresponds to Fig. 18a, and the blue band corresponds to Fig. 18b. Data are from RaDyO 2009, and represent the 20-min period starting 0400 UTC 8 Sep 2009.

transported downward by larger breakers and Langmuir circulations (Sullivan et al. 2007).

#### d. Wave coherence

SM15 showed that dissipation from individual breaking events is detectable.

To study the coherence of the dissipation measured by the IR imagery at the surface with the wave field, frequency spectra and cospectra of surface displacement and dissipation were calculated. An example of these is given in Fig. 17 for a 20-min period starting 0400 UTC 8 September 2009. Two regions of elevated squared coherence and associated phase can be seen: a low-frequency range with wave periods between 15 and 5 s and a high-frequency range with periods between approximately 4 and 2 s. The phase of the higher-frequency coherence peak suggests that the dissipation peaks approximately  $90^\circ$  after the wave peaks. At the lower-frequency peak, dissipation is  $180^\circ$  out of phase with the waves. Dissipation as a function of wave phase for the same time period is shown in Fig. 18. In this

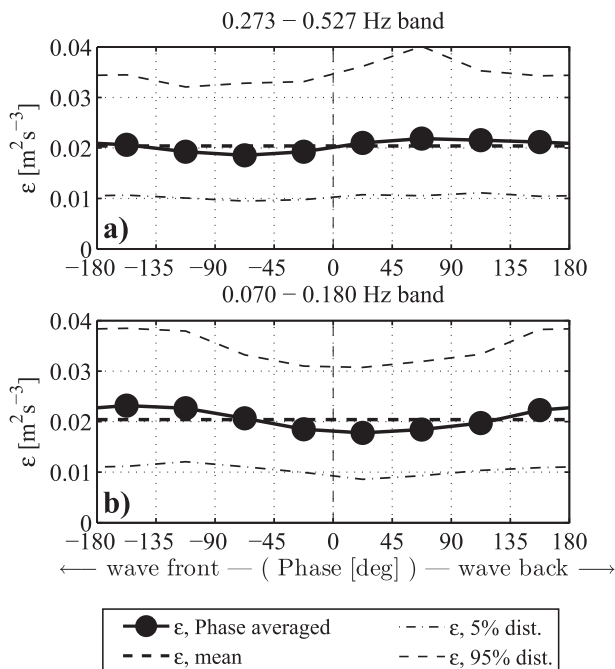


FIG. 18. Wave phase-averaged dissipation corresponding to the mean squared coherence peaks highlighted in Fig. 17. (a) Waves with periods between 1.9 and 3.7 s (red highlighting in Fig. 17) and (b) waves with periods between 5.6 and 14 s (blue highlighting in Fig. 17). The wave peak is at  $\theta = 0$ , and the wave is propagating to the left. Lines with circles are the mean dissipation in each wave phase bin, and the thick horizontal dashed lines indicate the mean dissipation. The lower and upper dashed lines indicate the 5th and 95th percentile, respectively, of the cumulative distribution function for each wave phase bin. Data are from RaDyO 2009 and represent the 20-min period starting 0400 UTC 8 Sep 2009.

figure, the surface displacement  $\eta(t)$  was first bandpass filtered to isolate the frequency range specified. The Hilbert transform  $H(t)$  of the filtered time series was computed, and the instantaneous wave phase was taken to be  $\theta(t) = \tan^{-1}[H(t)/\eta(t)]$ . Dissipation was then averaged over  $45^\circ$  bins of  $\theta$ . As expected, Fig. 18a shows that dissipation reaches a minimum  $90^\circ$  before the wave crest and a maximum  $90^\circ$  after, and Fig. 18b shows a dissipation maximum  $180^\circ$  out of phase with the waves. The phase-dependent signal is small compared to the mean dissipation in both cases. Wave phase dependence averaged for all three experiments showed similarly weak dependence of dissipation on wave phase (Fig. 19). However, the phase lag observed during HiRes 2010 was approximately  $0^\circ$ , unlike the approximately  $90^\circ$  of the other two experiments.

An important caveat to these measurements is the relatively large spatial scale over which the dissipation measurements were made. While the surface displacement was measured over an approximately  $10 \text{ cm} \times 10 \text{ cm}$  patch at the center of the reconstructed surface, the dissipation

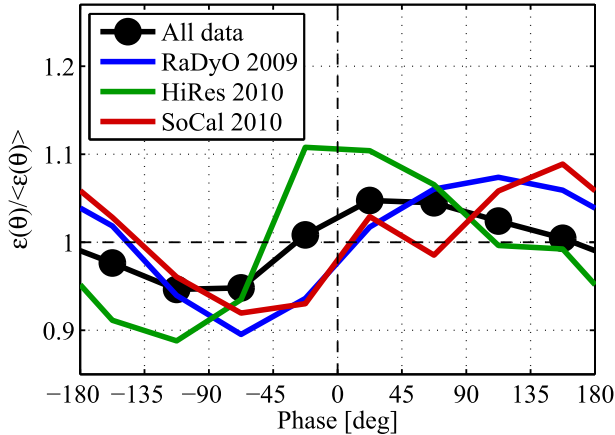


FIG. 19. Mean wave-phase dependence of normalized dissipation for the breaker-driven coherence band (red highlighting in Fig. 17). The black curve is an average of all data analyzed, and the blue, green, and red curves are from RaDyO 2009, HiRes 2010, and SoCal 2010, respectively. During HiRes 2010, surface dissipation was approximately in phase with the waves, while during the other two experiments, dissipation lagged the waves by approximately  $90^\circ$ .

measurements were calculated as an average over the entire regrided image, approximately  $2\text{ m} \times 2\text{ m}$ . This means that the shortest waves for which the phase dependence of the surface dissipation could theoretically be resolved are approximately 4 m in length, with a frequency of 0.6 Hz and phase speed of  $2.5\text{ m s}^{-1}$  (from the deep-water dispersion relation). Figure 6b shows the first moment of  $\Lambda(c)$ , which is the number of breaking fronts passing a given location per unit time per unit crest speed  $c$ . It can be seen that for all wave ages, the peak of  $c\Lambda(c)$  is found at phase speeds well below the phase speeds of the shortest waves resolved by the dissipation measurements. If the highest coherence of dissipation with wave phase is to be expected at wave scales where breaking is most common, then our dissipation measurements are averaged over too large a horizontal scale to resolve them. Furthermore, the large amount of dissipation associated with those small breakers (section 3) provides a “noisy background,” reducing the coherence of dissipation with the larger, resolved waves.

The strength of the phase-coherent signal observed here is in contrast with the observations by Gemmrich (2010) of significant dissipation enhancement at the wave crests. However, his wave conditions were strongly fetch limited with very low peak wave lengths and significant wave heights compared to the wave conditions of our experiments. Furthermore, the aforementioned scale limitation of our dissipation measurements mean that much of his dataset had peak wavelengths near our minimum resolvable scale.

The  $90^\circ$  phase lag at the wind-wave peak is not surprising. Figure 9 of SM15 shows an example time series

of dissipation during the passage of a large breaking wave. The dissipation immediately increases as the breaker passes and then slowly decays—in this case back to prebreaker levels within approximately one wave period. A dissipation time series starting with a step function at the wave peak, followed by decay, will result in a phase lag of between  $0^\circ$  and  $90^\circ$  depending on the ratio of dissipation time constant to wave period  $T_{\text{decay}}/T_{\text{wave}}$ . Another effect of having a large  $T_{\text{decay}}/T_{\text{wave}}$  ratio is that the difference between dissipation values at the wave peak versus the wave trough is reduced. This suggests that the stronger relative phase dependence observed for the HiRes 2010 data (green curve in Fig. 19) could be the result of a reduced  $T_{\text{decay}}/T_{\text{wave}}$ , producing both a the stronger wave phase dependence and a reduced phase lag.

The lower-frequency coherence peak that is  $180^\circ$  out of phase with the wave field is likely the result of a mechanism other than wave breaking. One potential explanation is the modification of background turbulence by wave motions. Veron et al. (2009) used rapid distortion theory to investigate the ratio of wave-coherent TKE to total TKE at the sea surface. Following the work of Townsend (1976) and Teixeira and Belcher (2002), they noted that this ratio could be approximated by

$$\frac{\langle \tilde{u}_1^2 \rangle}{\langle u_1^2 \rangle} \sim \frac{4}{5}ak + \frac{26}{35}(ak)^2, \quad (13)$$

where  $\langle u_1^2 \rangle$  is the variance of the turbulent velocity in the along-wave direction,  $\langle \tilde{u}_1^2 \rangle$  is variance of the wave-coherent component of the turbulent surface velocity in the along-wave direction, and  $ak$  is the wave slope. Using the significant wave height  $H_s = 2.3\text{ m}$  and the wavenumber of the spectral peak  $k_p = 0.06$ , where  $k_p$  is found by converting the peak in the frequency spectrum in Fig. 17 to the wavenumber using the deep-water dispersion relationship, the slope can be defined as  $ak = H_s k_p = 0.14$ . Dissipation,  $\varepsilon$ , can be related to TKE,  $\langle u^2 \rangle$ , by a time scale for decay of turbulence,  $T_\varepsilon$ , as  $\varepsilon \sim \langle u^2 \rangle / T_\varepsilon$ . Considering a narrow spectral band (as in Fig. 18b) places an upper bound on the decay time scales of both the wave-coherent and non-wave-coherent turbulence. If this constraint is extended to assume that the time scales of the wave-coherent and non-wave-coherent turbulence are similar, then the ratio of  $\tilde{\varepsilon}/\varepsilon$  is comparable to the ratio  $\langle \tilde{u}_1^2 \rangle / \langle u_1^2 \rangle$ . Thus, substituting  $ak$  into Eq. (13) gives a ratio of wave coherent to total dissipation of approximately  $\tilde{\varepsilon}/\varepsilon \sim 0.13$ . The amplitude of the phase-dependent signal in Fig. 18b can be taken to be the wave-coherent component of dissipation  $\tilde{\varepsilon} = 0.0026\text{ m}^2\text{ s}^{-3}$ , and the mean of the signal is the non-wave-coherent component

$\varepsilon = 0.021 \text{ m}^2 \text{ s}^{-3}$ . This results in a wave coherent to total dissipation ratio of  $\tilde{\varepsilon}/\varepsilon \sim 0.12$ , which is comparable to the value expected by rapid distortion theory. It should be noted that the rapid distortion theory assumes homogeneous, isotropic turbulence, which because of the observed rapid decay of dissipation with depth, we know to be not correct. It should also be noted that this low-frequency wave coherence peak was not a universal feature of the observations.

## 7. Conclusions

This work has been an investigation of TKE dissipation near the sea surface. To our knowledge, it represents the first measurements to extend subsurface TKE dissipation measurements all the way to the sea surface. Subsurface measurements were made with an array of pulse-coherent acoustic Doppler profilers, which were able to estimate dissipation at depths as close as 6 cm from the sea surface. Those measurements were then extended toward the surface, using the observed  $z^{-1}$  profile, to match surface measurements taken using stereo IR particle image velocimetry (PIV) SM15. This technique allowed us to estimate, and place limits upon, the total TKE dissipation in the near-surface region of the water column.

For depths below approximately one significant wave height from the sea surface, mean profiles of dissipation displayed an approximately  $z^{-2}$  dependence on depth and were within the scatter of the measurements of D96 and T96 when scaled by wave field dissipation. Closer to the surface, the dissipation profiles followed an approximately  $z^{-1}$  curve. However, these profiles showed dissipation levels elevated above wall layer levels by a factor that, somewhat counterintuitively, increased with increasing wave age.

Total integrated dissipation, over 20-min averaging periods, was found to agree well with dissipation by wave breaking for wave ages below approximately  $c_m/u_* = 50$  and winds above approximately  $U_{10} = 4 \text{ m s}^{-1}$ . This agreement was found over more than an order of magnitude of dissipation levels and suggests that wave breaking was the dominant source of turbulence in those conditions. During periods with older wave ages and lighter winds, measured water column TKE dissipation exceeded dissipation by breaking significantly.

Wave coherence of TKE dissipation at the surface was found to be consistent with breaking at the higher frequencies, where breaking events were more common. Although elevated dissipation by individual large breaking waves was clearly observed, the phase-coherence of waves and surface turbulence was overall not particularly strong. The instrument configuration, averaging dissipation over

an approximately  $2 \text{ m} \times 2 \text{ m}$  patch of the sea surface, precluded resolving the phase dependence of dissipation for waves smaller than approximately 4 m in length. However, since those unresolved smaller waves broke much more frequently, and supported a large fraction of dissipation, stronger coherence with dissipation is expected of them.

One of the fundamental results of the RaDyO and HiRes experiments is that TKE dissipation by wave breaking is far more concentrated near the sea surface than previously thought. The  $\Lambda(c)$  measurements of Sutherland and Melville (2013) showed that previous field measurements of breaking waves failed to capture non-air-entraining microbreakers. Using the framework of Phillips (1985) to estimate wave energy dissipation from  $\Lambda(c)$  measurements showed that a large fraction of wave energy was dissipated by these small breaking waves. While some of this turbulence is likely advected downward by other processes, typically larger breaking waves or Langmuir circulations, a thin layer of high dissipation near the surface would be the expected result. The elevated near-surface TKE dissipation observed in this work supports that hypothesis. When mean dissipation profiles were compared against the LES results of Sullivan et al. (2007), measured values were found to be elevated compared to modeled dissipation at shallow depths and reduced compared to modeled dissipation at deeper depths. This is likely because the breaking statistics used by the LES model failed to capture all of the small breaking waves, particularly microbreakers. Potentially very useful results could be produced by applying the  $\Lambda(c)$  measurements from Sutherland and Melville (2013) to LES simulations of the sort used by Sullivan et al. (2007). Results could then be compared directly with the measured TKE dissipation profiles as a check of our understanding of the breaker–Langmuir–turbulence–dissipation system.

The dynamics of the ocean surface boundary layer (OSBL) are the result of the complex interplay between many competing physical processes. LES remain one of the best tools available for untangling these interactions; however, for such simulations to be effective, they must include all relevant processes. Recent studies of modeling OSBL, for example, Belcher et al. (2012), have concentrated on scaling by the depth of the OSBL, suggesting that the evidence for the significance of the wave breaking turbulence is limited. However, the results of this paper find that the local dissipation in the upper OSBL may account for all or more of the local wind input to the wave field. Clearly there are apparent inconsistencies that will only be resolved by improved measurements and modeling.

Moving forward, the design of both modeling and measurement systems should endeavor to capture all relevant processes and spatiotemporal scales. Given the

dynamic ranges, covering scales from microbreakers to large entraining eddies, and the high intermittency associated with processes like wave breaking, this will stretch the limits of current instrumentation and models. The modeling side will require accurate inclusion of surface waves, breaking, Stokes drift due to directionally distributed wave fields, Langmuir circulations, buoyancy forcing, and wind forcing. It will be particularly important to resolve the elevated near-surface turbulence, not just for the dynamics but also for other processes like gas transfer that is coupled through air entrainment. On the observational side, future experiments, with new instruments better able to measure turbulence in the open sea within  $O(10)$  cm of the surface and down to the bottom of the OSBL to account for entrainment from below, will be needed.

Our work highlights the importance of TKE dissipation very near the sea surface and therefore the importance of better understanding the fluid dynamics and thermodynamics of this boundary with the atmosphere. However, at present, the uncertainties in both the measurements and the models do not permit a resolution of all the issues raised by the measurements.

*Acknowledgments.* These measurements would not have been possible without the excellent engineering and field support of Nick Statom and Luc Lenain. We also thank Tom Golfinos, Bill Gaines, and the crew of R/P *FLIP* for their tireless assistance, particularly with the somewhat unwieldy LTMI array. We thank Leonel Romero for providing the code for calculating wind input and wave field dissipation, as well as many useful discussions regarding those quantities, and Laurent Grare for processing meteorological data for the HiRes 2010 experiment. We also thank the two anonymous reviewers of this manuscript for their valuable contributions. This research was conducted under grants to WKM from the Office of Naval Research (Physical Oceanography, HiRes, and RaDyO DRIs) and the National Science Foundation (Ocean Sciences). During the revision and final preparation of this paper, PS was supported at Laboratoire d'Océanographie et du Climat by grants from the European Commission (PI Jean-Claude Gascard).

## APPENDIX A

### Aquadopp Processing Steps

Processing of Aquadopp PCADP data proceeded in the following steps:

1) The velocity range of pulse-coherent acoustic Doppler devices is inversely related to range and acoustic

frequency (Lacy and Sherwood 2004). The ambiguity velocities for the Aquadopps in the configuration used during these experiments were  $V_a = 0.13 \text{ m s}^{-1}$  for SoCal 2010,  $V_a = 0.15 \text{ m s}^{-1}$  for HiRes 2010, and approximately  $V_a \approx 0.32 \text{ m s}^{-1}$  for RaDyO 2009 (the data from RaDyO 2009 used the Aquadopp's on-board velocity ambiguity correction that gives a slightly wider velocity range). This velocity range is up to an order of magnitude lower than the wave orbital velocities during the experiment, so velocity unwrapping was imperative, particularly in the energetic near-surface region.

For each acoustic ping, the velocity difference between bins  $i$  and  $i + 1$ ,  $\delta u_i$ , was calculated. Whenever  $\delta u_i > V_a$  ( $\delta u_i < V_a$ ), the velocities at bins  $i + 1$  to  $N$  were reduced (increased) by  $2V_a$ .

- 2) Pulse-coherent correlation was used to remove spurious velocities. Correlation is affected by the number of scattering particles that are present in each sampling volume over two consecutive acoustic pings. Higher fluid velocities typically result in fewer groups of particles remaining in the sampling volume and thus lower correlation. In the high energy environment of this work, a low correlation threshold of 30% was chosen, and all data with correlations below that were removed.
- 3) For the vertical beams, velocity bin locations were transformed into surface-relative coordinates prior to structure function calculation. The surface elevation  $\eta(t)$  was taken from the stereo IR surface reconstruction at a location directly above the near-surface (fixed depth) LTMI. The surface-relative location of a sampling volume with a depth relative to the mean surface of  $z_{sv}(t)$  was then taken to be  $\zeta_{sv}(t) = z_{sv}(t) - \eta(t)$ . For the fixed depth LTMI, this was checked by tracking the strong surface reflection seen in the Aquadopp's backscatter amplitude data (cf. Gemmrich 2010). No wave measurements were available directly over the Aquadopp float, so surface tracking was used exclusively.
- 4) Structure functions were calculated at each velocity bin. The range of scales over which the structure functions were calculated was  $\delta x \leq r \leq r_{\max}$ , where  $\delta x$  is the velocity bin size, and  $r_{\max} = 0.12 \text{ m}$ . This value for  $r_{\max}$  was chosen as a scale typically smaller than the surface velocity integral length scale  $L$  (SM15). Locations where the full structure function could not be calculated, for example, within a distance  $r_{\max}$  of the surface in vertical beams (or within a distance  $r_{\max}$  of a beam end in the horizontal beams), were discarded.
- 5) At each depth bin, structure functions were averaged over 20 consecutive pings (10 s for SoCal 2010 and RaDyO 2009 and 5 s for HiRes 2010). These

averaged structure functions were then applied to Eqs. (8) and (9) to calculate dissipation at each bin.

## APPENDIX B

### Instrument Wakes in a Wave Field with a Mean Flow

It is instructive to attempt to estimate, very roughly, the levels of dissipation that might be expected in the wake of the LTMI.

Measurements by Lien and Sanford (2009) of dissipation in the wake of a cylindrical bridge piling produced an empirical nondimensional dissipation rate of

$$\frac{\varepsilon}{u_\infty^3/d} = 0.01(x_*/12)^{-3}, \quad (\text{B1})$$

or alternatively,

$$\frac{\varepsilon}{u_\infty^3/d} = 0.008e^{-(x_*-12)/10}, \quad (\text{B2})$$

with both curves producing comparably good fit to the data. Here,  $u_\infty$  is the far-field mean velocity,  $d$  is the diameter of the cylinder, and  $x_* = x/d$ , with  $x$  being the downstream distance from the cylinder. For  $x_*$  between 10 and 50, both of these empirical fits to the data give similar results.

Choosing the second of these relations and rewriting to solve for dissipation gives

$$\varepsilon = 0.008 \frac{u_\infty^3}{d} e^{-(x/d-12)/10}. \quad (\text{B3})$$

It is then possible to estimate the order of magnitude of dissipation found in the wake of an instrument. Using values from SoCal 2010 for the period starting 2300 UTC 6 December 2010 of  $H_s = 1.2$  m,  $T_p = 5.1$  s, and a mean LTMI depth of 1 m, linear theory would predict orbital motions, at the depth of the instrument, with a radius of 0.35 m and a speed of  $0.43 \text{ m s}^{-1}$ . Using  $d = 0.075$  m, the diameter of an Aquadopp,  $u_\infty = 0.43 \text{ m s}^{-1}$  and  $x = 2.2$  m, then gives a dissipation value of  $\varepsilon = 1.5 \times 10^{-3} \text{ m}^2 \text{ s}^{-3}$ .

While this estimate of dissipation in a wake is very simplistic, it does make the point that wake turbulence must be considered. The calculated wake dissipation is a similar order of magnitude to the strong intermittent events shown in Fig. 8 and is two orders of magnitude larger than the background dissipation level.

It should also be noted that the results of Lien and Sanford (2009) were for conditions with Reynolds numbers of  $O(10^7)$ , whereas the wake being discussed here

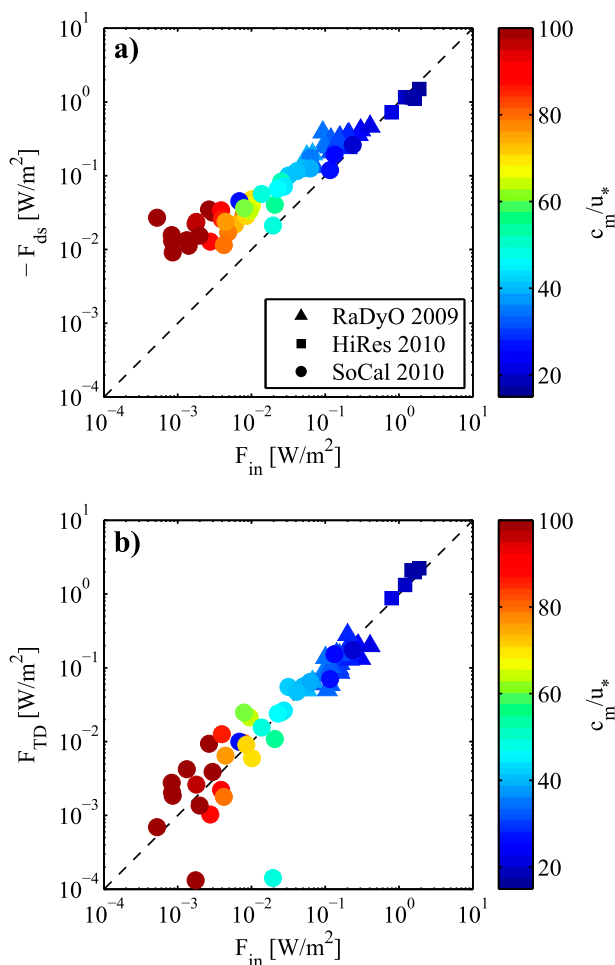


FIG. C1. Energy fluxes in the upper ocean. The abscissa in both panels is wind input from Snyder et al. (1981) as modified by The WAMDI Group (1988), based on the measured directional wave spectrum [see Eqs. (C2) and (C4)]. (a) The ordinate  $F_{ds}$  is the integrated spectral wave dissipation following Romero and Melville (2010), given by Eqs. (C3) and (C5). (b) The ordinate is the wind input as formulated by T96:  $F_{TD}$ , given by Eq. (C7).

has a Reynolds number  $O(10^4)$ . This difference may affect the nondimensionalized dissipation. The effects of vortex shedding have not been investigated, but at both Reynolds numbers, the Strouhal number would be similar, and turbulent vortex sheets would be expected in the wake (Lienhard 1966).

## APPENDIX C

### Energy Input Definitions

The evolution of the surface directional wave spectrum  $S_{\eta\eta}(k, \theta)$ , in the absence of currents, evolves according to

$$\frac{\partial}{\partial t} S_{\eta\eta}(k, \theta) + \mathbf{c}_g \cdot \nabla S_{\eta\eta}(k, \theta) = S_{\text{in}} + S_{\text{nl}} + S_{\text{ds}}, \quad (\text{C1})$$

where  $\mathbf{c}_g$  is the group velocity, and  $S_{\text{in}}$ ,  $S_{\text{nl}}$ , and  $S_{\text{ds}}$  are source terms corresponding to wind input, nonlinear energy transfer, and dissipation, respectively. The surface energy spectrum  $S_{\eta\eta}(k, \theta)$  is defined such that  $\langle \eta^2 \rangle = \int S_{\eta\eta}(k, \theta) k dk d\theta$ , where  $\eta$  is the surface displacement, and the angle brackets indicate spatial averaging. Integrating the source terms in Eq. (C1) gives energy flux (in units of watts per square meter) from the wind to the wave field,

$$F_{\text{in}} = \rho_w g \int S_{\text{in}}(k, \theta) k dk d\theta, \quad (\text{C2})$$

and wave energy dissipated:

$$F_{\text{ds}} = \rho_w g \int S_{\text{ds}}(k, \theta) k dk d\theta. \quad (\text{C3})$$

The  $S_{\text{nl}}$  term transfers energy between wavenumbers and integrates to zero.

In this work, the formulation of Snyder et al. (1981), as revised by The WAMDI Group (1988), was used to estimate wind input:

$$S_{\text{in}}(k, \theta) = 0.25 \frac{\rho_a}{\rho_w} \left( \frac{28u_*}{c} \cos\theta - 1 \right) \omega S_{\eta\eta}(k, \theta). \quad (\text{C4})$$

Wave dissipation was estimated using the spectral dissipation function of Romero and Melville (2010). This formulation uses an explicit balance between dissipation and input in the saturation range and an empirical dissipation function based on Alves and Banner (2003) at low and intermediate wavenumbers:

$$S_{\text{ds}}(k, \theta) = -C_{\text{ds}} \left[ \frac{B(k)}{B_r} \right]^{p/2} (E_{\text{ww}} k_{\text{ww}}^2)^m \left( \frac{k}{k_m} \right)^n \omega S_{\eta\eta}(k, \theta). \quad (\text{C5})$$

Here,  $B(k)$  is the azimuth-integrated saturation spectrum,  $E_{\text{ww}}$  is the total energy contained in the wind-wave spectrum,  $k_{\text{ww}}$  is the wavenumber of the peak of the wind-wave spectrum, and  $k_m$  is the mean wavenumber, related to the mean frequency [Eq. (1)] by the deep-water dispersion relation  $\omega_m^2 = gk_m$ . The function that enables saturation dependence is

$$p = \frac{p_0}{2} \left\langle 1 + \tanh \left\{ 10 \left[ \frac{B(k)}{B_r} \right]^{1/2} - 1 \right\} \right\rangle, \quad (\text{C6})$$

and  $C_{\text{ds}} = 9 \times 10^{-4}$ ,  $B_r = 2 \times 10^{-3}$ ,  $p_0 = 3.0$ ,  $m = 0.50$ , and  $n = 0.50$  are parameters from Romero and Melville (2010).

The energy flux used for scaling our dissipation measurements in Figs. 11 and 14,  $F_{\text{ds}}$  is the wave energy dissipation, given in Eq. (C3).

The data from T96 and D96, shown for comparison in Figs. 11 and 14, have been scaled by a slightly different energy flux. They used wind input, defined as

$$F_{\text{TD}} = \rho_w g \int \beta F(\omega, \theta) d\omega d\theta, \quad (\text{C7})$$

where  $\beta$  is from Donelan and Pierson (1987):

$$\beta = 0.194 \frac{\rho_a}{\rho_w} \left[ \frac{U_{\pi/k} \cos\theta}{c(k)} - 1 \right] \left| \frac{U_{\pi/k} \cos\theta}{c(k)} - 1 \right|. \quad (\text{C8})$$

In this formulation,  $U_{\pi/k}$  is the speed of the wind at a height of  $\pi/k$ , and  $c(k) = \sqrt{g/k}$ . Note that the wind input used in the original papers by T96 and D96 was defined such that it was equal to the  $F_{\text{TD}}$  used here divided by  $\rho_w$ .

A comparison of these energy flux estimates is given in Fig. C1. It can be seen that as the energy flux increases (in this case corresponding to increasing wind and decreasing wave age), agreement between all three estimates improves. In Fig. C1a, at high wave ages, dissipation by the wave field is as much as one order of magnitude higher than wind input. This is expected for a weakly forced, decaying wave field. Figure C1b shows that  $F_{\text{in}}$  and  $F_{\text{TD}}$  agree well at low wave ages, but scatter increases at higher wave ages. All wave ages from the T96 and D96 were in the range  $4 < c_p/u_* < 29$ , suggesting that  $-F_{\text{ds}}$  and  $F_{\text{TD}}$  would agree well for their data (plotted in Fig. 11).

## REFERENCES

- Agrawal, Y. C., E. A. Terray, M. A. Donelan, P. A. Hwang, A. J. Williams III, W. M. Drennan, K. K. Kahma, and S. A. Krtaigorodskii, 1992: Enhanced dissipation of kinetic energy beneath surface waves. *Nature*, **359**, 219–220, doi:10.1038/359219a0.
- Alves, J. H. G. M., and M. L. Banner, 2003: Performance of a saturation-based dissipation-rate source term in modeling the fetch-limited evolution of wind waves. *J. Phys. Oceanogr.*, **33**, 1274–1298, doi:10.1175/1520-0485(2003)033<1274:POASDS>2.0.CO;2.
- Anis, A., and J. Moum, 1992: The superadiabatic surface layer of the ocean during convection. *J. Phys. Oceanogr.*, **22**, 1221–1227, doi:10.1175/1520-0485(1992)022<1221:TSSL0T>2.0.CO;2.
- Ardhuin, F., B. Chapron, and F. Collard, 2009: Observation of swell dissipation across oceans. *Geophys. Res. Lett.*, **36**, L06607, doi:10.1029/2008GL037030.
- Belcher, S. E., and Coauthors, 2012: A global perspective on Langmuir turbulence in the ocean surface boundary layer. *Geophys. Res. Lett.*, **39**, L18605, doi:10.1029/2012GL052932.
- Brodtkorb, P., P. Johannesson, G. Lindgren, I. Rychlik, J. Rydén, and E. Sjö, 2000: WAFO—A Matlab toolbox for the analysis

- of random waves and loads. *Proc. 10th Int. Offshore and Polar Eng. Conf.*, Vol. 3, Seattle, WA, ISOPE, 343–350.
- Craig, P. D., and M. L. Banner, 1994: Modeling wave-enhanced turbulence in the ocean surface layer. *J. Phys. Oceanogr.*, **24**, 2546–2559, doi:10.1175/1520-0485(1994)024<2546:MWETIT>2.0.CO;2.
- Dickey, T., and Coauthors, 2012: Introduction to special section on recent advances in the study of optical variability in the near-surface and upper ocean. *J. Geophys. Res.*, **117**, C00H20, doi:10.1029/2012JC007964.
- Donelan, M. A., and W. J. Pierson, 1987: Radar scattering and equilibrium ranges in wind-generated waves with application to scatterometry. *J. Geophys. Res.*, **92**, 4971–5029, doi:10.1029/JC092iC05p04971.
- Drzen, D. A., W. K. Melville, and L. Lenain, 2008: Inertial scaling of dissipation in unsteady breaking waves. *J. Fluid Mech.*, **611**, 307–332, doi:10.1017/S0022112008002826.
- Drennan, W., M. Donelan, E. Terray, and K. Katsaros, 1996: Oceanic turbulence dissipation measurements in SWADE. *J. Phys. Oceanogr.*, **26**, 808–815, doi:10.1175/1520-0485(1996)026<0808:OTDMIS>2.0.CO;2.
- Gargett, A. E., 1989: Ocean turbulence. *Annu. Rev. Fluid Mech.*, **21**, 419–451, doi:10.1146/annurev.fl.21.010189.002223.
- Gemmrich, J. R., 2010: Strong turbulence in the wave crest region. *J. Phys. Oceanogr.*, **40**, 583–595, doi:10.1175/2009JPO4179.1.
- , M. L. Banner, and C. Garrett, 2008: Spectrally resolved energy dissipation rate and momentum flux of breaking. *J. Phys. Oceanogr.*, **38**, 1296–1312, doi:10.1175/2007JPO3762.1.
- Grant, A. L. M., and S. E. Belcher, 2009: Characteristics of Langmuir turbulence in the ocean mixed layer. *J. Phys. Oceanogr.*, **39**, 1871–1887, doi:10.1175/2009JPO4119.1.
- Grare, L., L. Lenain, and W. K. Melville, 2013: Wave-coherent airflow and critical layers over ocean waves. *J. Phys. Oceanogr.*, **43**, 2156–2172, doi:10.1175/JPO-D-13-056.1.
- Jessup, A. T., and K. R. Phadnis, 2005: Measurement of the geometric and kinematic properties of microscale breaking waves from infrared imagery using a PIV algorithm. *Meas. Sci. Technol.*, **16**, 1961–1969, doi:10.1088/0957-0233/16/10/011.
- Kitaigorodskii, S., M. Donelan, J. Lumley, and E. Terray, 1983: Wave-turbulence interactions in the upper ocean. Part II. Statistical characteristics of wave and turbulent components of the random velocity field in the marine surface layer. *J. Phys. Oceanogr.*, **13**, 1988–1999, doi:10.1175/1520-0485(1983)013<1988:WTITU>2.0.CO;2.
- Kleiss, J. M., and W. K. Melville, 2010: Observations of wave breaking kinematics in fetch-limited seas. *J. Phys. Oceanogr.*, **40**, 2575–2604, doi:10.1175/2010JPO4383.1.
- Kolmogorov, A. N., 1991: The local structure of turbulence in incompressible viscous fluid for very large Reynolds numbers. *Proc. Roy. Soc. London*, **A434**, 9–13, doi:10.1098/rspa.1991.0075.
- Lacy, J. R., and C. R. Sherwood, 2004: Accuracy of a pulse-coherent acoustic Doppler profiler in a wave-dominated flow. *J. Atmos. Oceanic Technol.*, **21**, 1448–1461, doi:10.1175/1520-0426(2004)021<1448:AOAPAD>2.0.CO;2.
- Lien, R.-C., and T. Sanford, 2009: Vorticity and turbulence in the wake of a bridge pier. *IEEE J. Oceanic Eng.*, **34**, 307–314, doi:10.1109/JOE.2009.2019383.
- Lienhard, J. H., 1966: Synopsis of lift, drag, and vortex frequency data for rigid circular cylinders. Washington State University Bull. 300, 32 pp. [Available online at [www.uh.edu/engines/vortexcylinders.pdf](http://www.uh.edu/engines/vortexcylinders.pdf).]
- Melville, W. K., 1994: Energy dissipation in breaking waves. *J. Phys. Oceanogr.*, **24**, 2041–2049, doi:10.1175/1520-0485(1994)024<2041:EDBBW>2.0.CO;2.
- , 1996: The role of surface-wave breaking in air-sea interaction. *Annu. Rev. Fluid Mech.*, **28**, 279–321, doi:10.1146/annurev.fl.28.010196.001431.
- , and P. Matusov, 2002: Distribution of breaking waves at the ocean surface. *Nature*, **417**, 58–63, doi:10.1038/417058a.
- , F. Veron, and C. J. White, 2002: The velocity field under breaking waves: Coherent structures and turbulence. *J. Fluid Mech.*, **454**, 203–233, doi:10.1017/S0022112001007078.
- Mollo-Christensen, E., 1968: Wind tunnel test of the superstructure of the R/V Flip for assessment of wind field distortion. MIT Fluid Dynamics Research Laboratory, 34 pp.
- Phillips, O. M., 1985: Spectral and statistical properties of the equilibrium range in wind-generated gravity waves. *J. Fluid Mech.*, **156**, 505–531, doi:10.1017/S0022112085002221.
- Rapp, R. J., and W. K. Melville, 1990: Laboratory measurements of deep-water breaking waves. *Philos. Trans. Roy. Soc. London*, **A331**, 735–800, doi:10.1098/rsta.1990.0098.
- Rasche, N., B. Chapron, F. Ardhuin, and A. Soloviev, 2013: A note on the direct injection of turbulence by breaking waves. *Ocean Modell.*, **70**, 145–151, doi:10.1016/j.ocemod.2012.09.001.
- Romero, L., and W. K. Melville, 2010: Numerical modeling of fetch-limited waves in the Gulf of Tehuantepec. *J. Phys. Oceanogr.*, **40**, 466–486, doi:10.1175/2009JPO4128.1.
- , —, and J. M. Kleiss, 2012: Spectral energy dissipation due to surface-wave breaking. *J. Phys. Oceanogr.*, **42**, 1421–1444, doi:10.1175/JPO-D-11-072.1.
- Schwendeman, M. S., J. Thomson, and J. R. Gemmrich, 2014: Wave breaking dissipation in a young wind sea. *J. Phys. Oceanogr.*, **44**, 104–127, doi:10.1175/JPO-D-12-0237.1.
- Smith, J. A., and K. F. Rieder, 1997: Wave induced motion of flip. *Ocean Eng.*, **24**, 95–110, doi:10.1016/0029-8018(96)00008-X.
- Snyder, R. L., F. W. Dobson, J. A. Elliott, and R. B. Long, 1981: Array measurements of atmospheric pressure fluctuations above surface gravity waves. *J. Fluid Mech.*, **102**, 1–59, doi:10.1017/S0022112081002528.
- Soloviev, A., and R. Lukas, 2003: Observation of wave-enhanced turbulence in the near-surface layer of the ocean during TOGA COARE. *Deep-Sea Res. I*, **50**, 371–395, doi:10.1016/S0967-0637(03)00004-9.
- Sullivan, P. P., J. C. McWilliams, and W. K. Melville, 2004: The oceanic boundary layer driven by wave breaking with stochastic variability. Part 1. Direct numerical simulations. *J. Fluid Mech.*, **507**, 143–174, doi:10.1017/S0022112004008882.
- , —, and —, 2007: Surface gravity wave effects in the oceanic boundary layer: Large-eddy simulation with vortex force and stochastic breakers. *J. Fluid Mech.*, **593**, 405–452, doi:10.1017/S002211200700897X.
- Sutherland, G., B. Ward, and K. H. Christensen, 2013: Wave-turbulence scaling in the ocean mixed layer. *Ocean Sci.*, **9**, 597–608, doi:10.5194/os-9-597-2013.
- , K. H. Christensen, and B. Ward, 2014: Evaluating Langmuir turbulence parameterizations in the ocean surface boundary layer. *J. Geophys. Res.*, **119**, 1899–1910, doi:10.1002/2013JC009537.
- Sutherland, P., and W. K. Melville, 2013: Field measurements and scaling of ocean surface wave-breaking statistics. *Geophys. Res. Lett.*, **40**, 3074–3079, doi:10.1002/grl.50584.

- Teixeira, M. A. C., and S. E. Belcher, 2002: On the distortion of turbulence by a progressive surface wave. *J. Fluid Mech.*, **458**, 229–267, doi:[10.1017/S0022112002007838](https://doi.org/10.1017/S0022112002007838).
- Terray, E. A., M. A. Donelan, Y. C. Agrawal, W. M. Drennan, K. K. Kahma, A. J. Williams III, P. A. Hwang, and S. A. Kitaigorodskii, 1996: Estimates of kinetic energy dissipation under breaking waves. *J. Phys. Oceanogr.*, **26**, 792–807, doi:[10.1175/1520-0485\(1996\)026<0792:EOKEDU>2.0.CO;2](https://doi.org/10.1175/1520-0485(1996)026<0792:EOKEDU>2.0.CO;2).
- The WAMDI Group, 1988: The WAM model—A third generation ocean wave prediction model. *J. Phys. Oceanogr.*, **18**, 1775–1810, doi:[10.1175/1520-0485\(1988\)018,1775:TWMTO>2.0.CO;2](https://doi.org/10.1175/1520-0485(1988)018,1775:TWMTO>2.0.CO;2).
- Thomson, J., 2012: Wave breaking dissipation observed with “SWIFT” drifters. *J. Atmos. Oceanic Technol.*, **29**, 1866–1882, doi:[10.1175/JTECH-D-12-00018.1](https://doi.org/10.1175/JTECH-D-12-00018.1).
- Townsend, A. A., 1976: *The Structure of Turbulent Shear Flow*. 2nd ed. Cambridge University Press, 429 pp.
- Veron, F., W. K. Melville, and L. Lenain, 2009: Measurements of ocean surface turbulence and wave-turbulence interactions. *J. Phys. Oceanogr.*, **39**, 2310–2323, doi:[10.1175/2009JPO4019.1](https://doi.org/10.1175/2009JPO4019.1).
- Wiles, P. J., T. P. Rippeth, J. H. Simpson, and P. J. Hendricks, 2006: A novel technique for measuring the rate of turbulent dissipation in the marine environment. *Geophys. Res. Lett.*, **33**, L21608, doi:[10.1029/2006GL027050](https://doi.org/10.1029/2006GL027050).